Water Resources Research

RESEARCH ARTICLE
10.1029/2022WR033440

An Examination of Water-Related Melt Processes in Arctic Snow on Tundra and Sea-Ice

Anika Pinzner[1], Matthew Sturm[1], Jennifer S. Delamere[1], and Andrew R. Mahoney[1]

[1]Geophysical Institute, University of Alaska Fairbanks, Fairbanks, AK, USA

Key Points:

- Water-related processes in snow can promote or impede lateral advection of heat and mass, enhancing or inhibiting melt in the Arctic
- The composition and topography of the substrate govern the nature of the water-snow interactions and thereby influence meltout patterns
- The most rapid and largest changes in surface albedo happen just prior to the snow-free date when water-snow melt mechanisms reach a peak

Correspondence to:

A. Pinzner,
apinzner@alaska.edu

Citation:

Pinzner, A., Sturm, M., Delamere, J. S., & Mahoney, A. R. (2024). An examination of water-related melt processes in Arctic snow on tundra and sea-ice. *Water Resources Research*, *60*, e2022WR033440. https://doi.org/10.1029/2022WR033440

Received 10 AUG 2022
Accepted 5 DEC 2023

Author Contributions:

Conceptualization: Anika Pinzner, Matthew Sturm, Andrew R. Mahoney
Data curation: Anika Pinzner
Funding acquisition: Matthew Sturm, Jennifer S. Delamere
Investigation: Matthew Sturm, Jennifer S. Delamere, Andrew R. Mahoney
Methodology: Anika Pinzner, Matthew Sturm, Jennifer S. Delamere, Andrew R. Mahoney
Project Administration: Matthew Sturm
Software: Anika Pinzner, Matthew Sturm, Jennifer S. Delamere, Andrew R. Mahoney
Supervision: Matthew Sturm, Andrew R. Mahoney
Writing – original draft: Anika Pinzner, Matthew Sturm

Abstract From April through June in 2019 and 2022, we monitored snow melt at three sites near Utqiaġvik, Alaska. Along 200-m lines we measured snow depth, density, stratigraphy, snow-covered area, and spectral albedo. Site 1 (ARM) was sloped tundra drained by water tracks. Site 2 (BEO) was flat polygonal tundra. Site 3 (ICE) was on undeformed landfast sea ice. All three sites were within a 6 km radius. Despite similar pre-melt snow distributions and weather, the melt progression differed markedly between sites. In 2019, by mid-melt, there was 40% less snow-covered area at ARM versus ICE, and 34% less snow-covered area at ARM versus BEO. The 2022 melt started 2 weeks later than in 2019 and was rapid, so smaller differences in snow-covered areas developed. In both years meltout dates varied by up to 25 days between sites, and more than 20 days within sites, with melt rates at locations only meters apart differing by up to a factor of seven. This melt diachroneity led to highly heterogeneous meltout patterns at all three sites. Our measurements and observations indicate that, in addition to reductions in snow reflective properties and wind-driven heat advection, the fate of meltwater plays a key role in producing melt diachroneity. We identify seven snow-water mechanisms that can enhance or inhibit melt rates, all largely controlled by the local topography and the nature of the substrate. These mechanisms are important because the most rapid changes in albedo coincide with the peak of water-snow melt interactions.

Plain Language Summary We observed in detail snow melt on two different tundra locations and one sea ice location in Arctic Alaska in the spring of 2019 and 2022. During the melt season, these landscapes go from reflecting over 80% of the sunlight to less than 20%, a transition that impacts the global climate. Our observations showed that while warming weather is what ultimately controls snowmelt, the re-freezing and flow of meltwater within the snowpack, plays a crucial role in controlling local melt rates of individual snow patches. These water-related melt mechanisms, together with wind-driven laterally advected air and the reflective properties of the snow, largely control the date individual snow patches disappear, and therefore, when the most rapid changes in solar reflectivity will take place.

1. Introduction

The term breakup in the Arctic denotes the abrupt transition from winter to summer when the snow rapidly melts away and the ice covering Arctic lakes, rivers, and seas breaks apart and drifts off. Breakup imposes a major alteration in the way Arctic residents move about (from skis and tracked vehicles to wheels and boats) and in the activities in which they engage. In a matter of days, the Arctic landscape sheds its white winter shroud, taking on the browns and greens of the tundra and the blues and turquoise of the melting sea ice.

The transition to a snow-free surface is fast in the Arctic for three reasons: (a) Snowpacks on Arctic sea ice and tundra are thin, often only 30–50 cm in depth (Sturm & Liston, 2021); (b) Arctic snowpacks experience a drastic increase in incoming solar radiation as the melt progresses (e.g., Sánchez & McInnes, 2015); and (c) much of the Arctic snow is at low elevations and experiences only limited night cooling due to the long daylight hours of the Arctic spring.

This change from snow-covered to snow-free surfaces is concomitant with a rapid decrease in broadband albedo (α) of Arctic landscapes in spring. Snow-covered areas with high albedo values of around 0.8 (Doherty et al., 2013; Warren, 1982) are replaced by seawater ($\alpha \sim 0.1$) and tundra ($\alpha \sim 0.2$) which leads to a drastic increase in solar absorption (Callaghan et al., 2011; Marcianesi et al., 2021). It is this albedo transition that underlies the ice-albedo feedback mechanism associated with the rapidly warming Arctic climate (Curry et al., 1995; Liston & Hiemstra, 2011).

Writing – review & editing: Anika Pinzner, Matthew Sturm, Jennifer S. Delamere, Andrew R. Mahoney

With Arctic tundra covering about 12 million km^2 of the earth and Arctic sea ice an additional 14 million km^2 at maximum extent (Perovich et al., 2020), melt-driven albedo transitions on these surface covers thus have the potential to alter not only the regional but also the global climate.

During two snow melt seasons near the Arctic community of Utqiaġvik, Alaska, we observed that water-snow melt mechanisms contributed to the rate at which snow disappeared to reveal the tundra or sea ice beneath (Figure 1). Many of the mechanisms we observed significantly affect local melt rates and therefore the transition from highly reflective to highly absorptive surfaces. Differences in meltout dates at adjacent patches varied by as much as 3 weeks despite similar pre-melt snow conditions. The net result was an extremely patchy albedo landscape. Closer examination revealed that these water-snow mechanisms initially involved the development of internal and superimposed ice masses, and later water flowing through and beneath the snow. Consequently, the mechanisms were tightly coupled to the topography of the substrate beneath the snow.

2. Diachroneity of Arctic Snowmelt

Dingman (2008) describes a series of three distinct phases of the meltout process, which serve as a useful framework for understanding the progression of snowmelt over time. It is often applied at basin scales to assess inter-annual variability in the melt (e.g. Colombo et al., 2019) or to predict the timing and magnitude of run-off (e.g. Jost et al., 2012). Here, it is also useful for understanding the varying progress of melt between individual snow patches.

In addition to an accumulation period prior to the onset of melt (Phase 0), Dingman (2008) identified the three phases of Arctic snowmelt based on changes in the heat balance of the snowpack: (a) a warming phase as the snowpack temperature rises to 0°C (Phase 1), (b) a ripening phase, when meltwater generated at the surface is retained in the pack and refreezes (Phase 2), and (c) an output phase where water drains from the snow as additional heat energy is absorbed (Phase 3). Vérin et al. (2022) have suggested a similar sequence for snowmelt on sea ice. In this study, we will use the melt sequence approach to compare the general progression of the 2019 and 2022 melt seasons near Utqiaġvik, AK.

Applying the melt-phase framework on a snow-patch scale allows us to examine the drivers of the melt spatially. On the snow patch scale (e.g., one to several tens of meters), the melt evolution can be highly variable, with adjacent patches being in different phases of the melt. The extreme melt heterogeneity emphasizes the need for an associated concept with the melt sequence: *diachroneity*. Diachroneity, a term commonly used in geology, encompasses the idea that similar processes will take place at different times in different areas (e.g., Benson, 1960; Gold et al., 2009; Lam et al., 2022). Applied to Dingman's concept of melt phases for Arctic snowmelt, diachroneity means that adjacent snow patches might melt asynchronously. For each patch, a melt phase might be of longer or shorter duration than for its nearest neighbor as the melt evolves, leading to different melt phases being underway at the same time.

Three main factors lead to snowmelt diachroneity: (a) variations in the pre-melt snow distribution and properties, a result of winter snow deposition processes, (b) the nature and topography of the underlying substrate, and (c) laterally advected energy (moving with either air or water) which is often topographically driven.

The pre-melt snow conditions such as snow depth, density, and temperature, are represented in Dingman's melt framework (Phase 0) as the cold content of the snow, which Parajuli et al. (2021) define as “an internal energy state within a snowpack.” Here, we argue that similar properties of the underlying substrate also strongly influence the melt progression. In particular, the bulk temperature, thermal conductivity, and heat capacity of the substrate material determine the rate at which meltwater reaching the base of the snowpack can refreeze, how much meltwater can be refrozen, and how much the overlying snow cools or warms (Domine et al., 2016; Park et al., 2018; Schwerdtfecer, 1963). The capacity of the substrate to refreeze meltwater is thus essential in determining melt rates and meltout patterns, as the movement of water, whether it refreezes locally versus drains laterally determines the magnitude of the advection of heat laterally and therefore melt rates spatially.

Horizontal advection processes can drastically alter the energy balance of a snow patch, accelerating, decelerating, or even reversing the progression through the melt stages and thus greatly increase melt diachroneity. Considerable attention has been given to warm air advection from bare tundra (cf. Van der Valk et al., 2022), where eight-fold horizontal differences in albedo (e.g., bare tundra adjacent vs. snow) can lead to accelerated snow

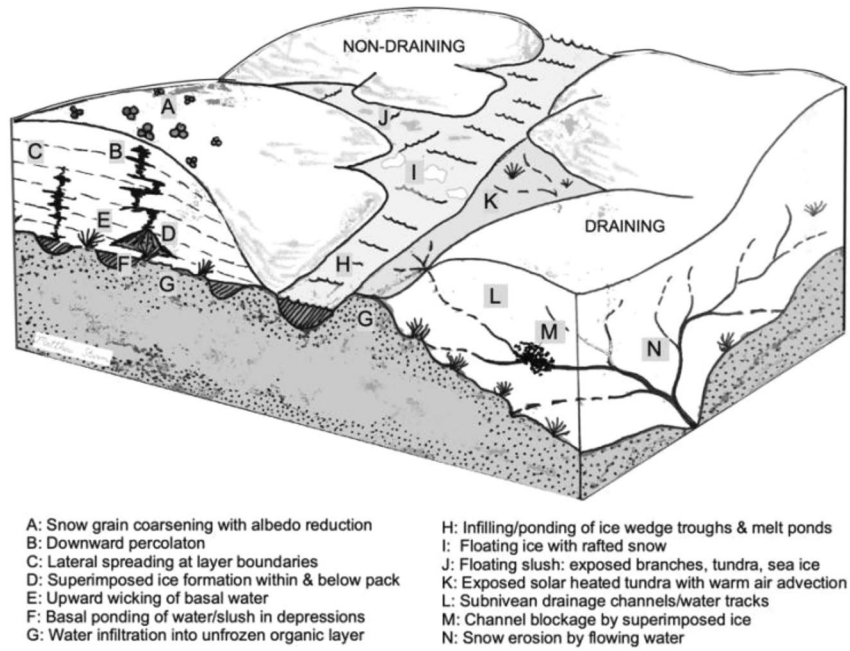

Figure 1. A schematic of mechanisms involving water and snow that can enhance or diminish snow melt rates.

melt along patch edges. On the contrary, cold and dry windy conditions, for example, have been shown to lead to a strongly negative effect on the snow's surface energetics, inhibiting melt (Harder et al., 2019; Van Mullem & Garen, 2004). While direct measurements and modeling of advected turbulent sensible and latent heat remain challenging, several studies conclude that wind-driven lateral heat advection can significantly affect snow melt rates. The contribution has been estimated to range from 5% to 40% of the total melt (Harder et al., 2019; Liston, 1995; Schlögl et al., 2018; Van der Valk et al., 2022; Van Mullem & Garen, 2004).

Here, we focus on another advective process that has received less attention—*the movement of water within and under the snow*. Figure 1 shows some of the many ways in which the movement of water within a snow patch or between patches can affect melt evolution. Once water is introduced to the snowpack, the cold content of the pack and underlying substrate as well as the slope of the latter, are key factors determining the fate of the water and therefore the impact on the local melt progression. In this way, water-related advective processes are similar to advective wind-driven heat transfer processes, where surface roughness and local topography, along with snow patch size and geometry, play a key role in determining the magnitude of the advected melt component (Harder et al., 2019; Van der Valk et al., 2022). These two advective processes, water-driven and wind-driven, further are linked and can reinforce or weaken each other and thus accelerate (positive feedback loop) or decelerate (negative feedback loop) the melt.

This paper explores how diachroneity affects the Dingman melt phases, which serve as a framework for comparing the general progression of the two melt seasons (e.g., 2019 and 2022). Our key focus is on the water-related melt mechanisms we observed. We describe how they led to both increased and decreased melt rates at local scales, which in turn caused considerable melt diachroneity and the enhanced patchiness of Arctic snowmelt patterns.

3. Study Area

The study was conducted in a coastal environment near Utqiaġvik, AK (Figure 2) at three sites close to locations used by Grenfell and Perovich (2004) for albedo measurements. In April 2019 and again in 2022, we established a 200 × 20-m swath for snow measurements at each site. The ARM site (Figure 3, 71.322°N, 156.612°W) at the Department of Energy's North Slope of Alaska (NSA) Atmospheric Radiation Measurement (ARM) Observatory (https://www.arm.gov/capabilities/observatories/nsa) is gently sloping tundra drained by eight water tracks, immature drainage channels common throughout the Arctic (König & Sturm, 1998; Parr et al., 2020; Trochim

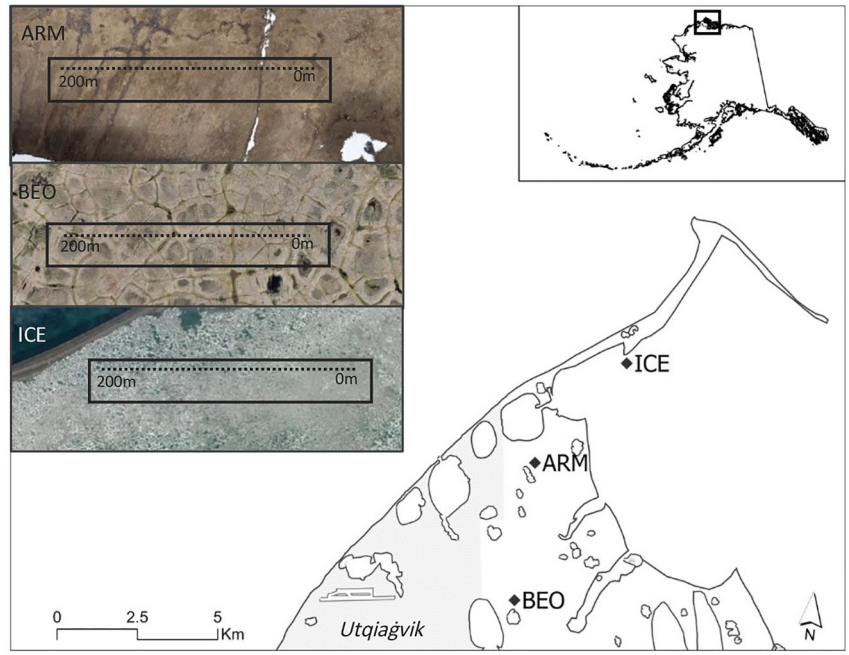

Figure 2. The three locations where we monitored snow melt near Utqiaġvik, AK: ARM, BEO, and ICE. The measurement swaths (outlined in black) are 20 by 200 m; along the northern edge of each swath, we measured snow depth at 1-m and albedo at 5-m intervals (dotted lines).

et al., 2016). The BEO site (Figure 4, 71.284°N 156.632°W) at the Barrow Environmental Observatory (https://eu-interact.org/field-sites/barrow-arctic-research-centerenvironmental-observatory/) is flat polygonal tundra, mostly low-centered polygons, cut by a dozen ice-wedge troughs. The ICE site (Figure 5, 71.349°N 156.530°W) was situated on the flat undeformed landfast sea ice of Elson Lagoon.

Alluviomarine deposits (Farquharson et al., 2016) underlie the tundra sites and much of the coastal plain of Alaska's North Slope (Frost et al., 2018). These deposits develop "patterned-ground" due to intensive frost action, producing a tundra surface of nested topographic scales with micro (tussock scale), meso (ice wedge scale), and macro (hillslope) features. Using a combination of classification systems (Table 1, cf. Lara et al., 2015, 2018; Walker et al., 1980; Washburn, 1956) with the addition of two categories for drainage, we have classified the sites (Figures 3 and 4). We differentiated high-centered polygons (HCPs) from flat-high-centered polygons (FHCPs) and low-centered polygons (LCPs) from flat-low-centered polygons (FLCPs) based on whether the rim-to-lowest

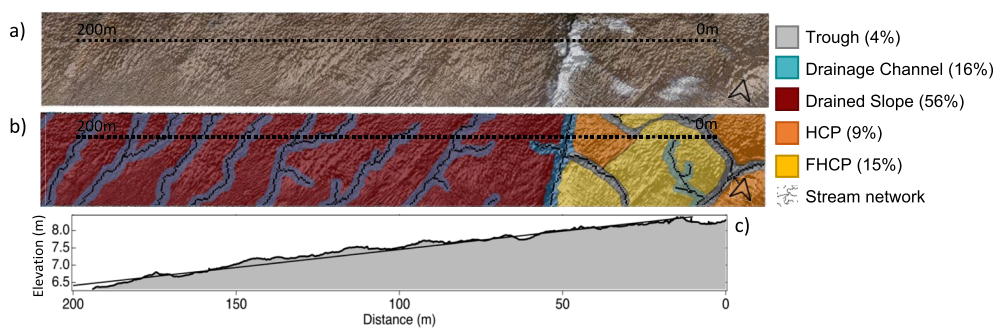

Figure 3. The ARM site. (a) An orthomosaic from 15 June 2019 underlain by a hillshade map. The dashed line is the 200-m line along which albedo and snow depth measurements were made, We started measuring at the east end (0 m). The lack of any ponded water is notable. (b) Landform map showing eight water tracks (blue) draining the site. A small area of polygonal ground is found at the east end of the line. The hydrologic flow network for ARM is shown in black. (c) A surface elevation profile along the 200-m measurement line overlain by a third-degree polynomial regression line to emphasize the general surface topography trend. Landform percentages are shown in the key.

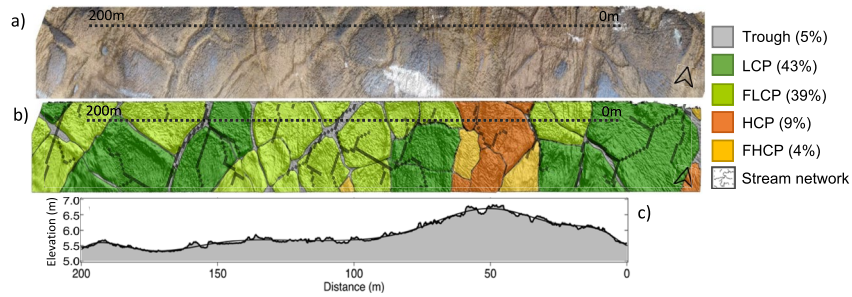

Figure 4. The BEO site. (a) Same as Figure 3 (orthomosaic image from 17 June 2019). The gray areas are water ponded in LCPs and troughs. (b) Landform map showing how LCPs and FLCPs dominate this area. The hydrologic flow network for BEO is shown in black. (c) A surface elevation profile along the 200-m measurement line and a third-degree polynomial regression line. Landform percentages are shown in the key.

point of the polygon exceeded 0.5 m. The types of tundra found at ARM and BEO cover 70% of the 60,000 km^2 Arctic Coastal Plain (Lara et al., 2018).

At ICE, the substrate topography changed as the melt progressed. Sixty years ago, Hanson (1961) reported on the development of melt ponds on sea ice. Follow-on studies (e.g., Eicken, 1994; Polashenski et al., 2017; Webster et al., 2022) have continued to explore these features and their role in climate. The close association between the location of melt ponds with pre-melt snow dune distribution has been well established (e.g., Petrich et al., 2012), and the strong correlation between ponds forming in the interstices of snow dunes and following the snow depth contours was also seen in our study (ibid, Figure 5).

The hydrological flow network at the sites (overlain on panels (b) in Figures 3–5) was determined using Lidar Datasets at NOAA Digital Coast Lidar (2019) and digital elevation models (DEMs) derived from structure-from-motion photography. Flow paths were delineated using the hydrology toolkit in QGIS 3.12.1-București (2020). At ARM, these flow pathways tended to be straight and located in relatively shallow channels. At BEO, the polygonal ground created meandering flow paths that followed the ice trough networks. Using the same tools at ICE and the pre-melt DTM as a basis, the flow network showed a series of melt ponds and connecting streams oriented east-west with a characteristic pinch-and-swell configuration. Not shown in Figure 5, but evident in the aerial photography and snow pit observations, ponded water was abundant later in the melt at BEO, where ponding was found mostly in low-centered polygons and troughs. Ponds were also prevalent at ICE, but not at ARM.

4. Measurements and Methods

4.1. Snow Depth and Properties

We used in situ and aerial methods to track the snowmelt (Table 2). During near-daily visits to each site, measurements of snow stratigraphy, density, liquid water, and superimposed ice were made in snow pits and trenches.

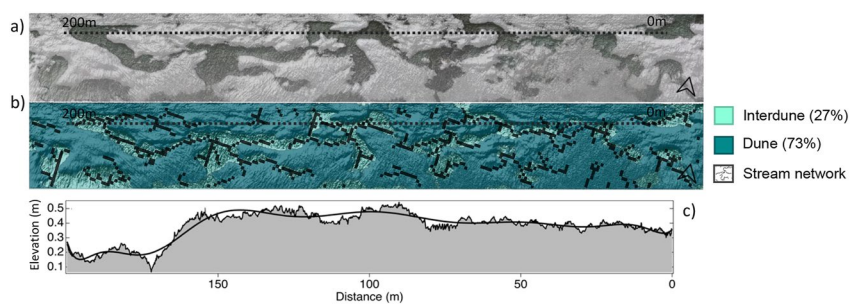

Figure 5. The ICE site. (a) An orthomosaic from 16 June 2019 underlain by a hillshade map. Snow dunes (bright) and melt ponds (dark) can be readily differentiated. (b) Landform maps showing dune (dark) and interdune (light) areas. The hydrologic flow network for ICE is shown in black. (c) We substracted snow depth measurements from the snow surface on 24 May to produce the ice surface elevation along the 200-m line and overlaid it by a third-degree polynomial regression line (black line). The small depression (~0.2 m) in the ice surface at 170 m later became a pond.

Table 1
Landform Classes With Corresponding Capacity to Retain Water and Residence Time of Water

Class	Water-holding capacity	Residence time
High-Centered Polygon (HCP)	Low	Short
Flat-High-Centered Polygon (FHCP)	Low	Short
Low-Centered Polygon (LCP)	High	Long
Flat-Low-Centered Polygon (FLCP)	High	Long
*Trough Networks	High	Long
Drained Slopes	Low	Short
*Water Tracks	High	Medium

Note. * Categories new in this study.

These measurements, being destructive, did not allow us to produce stratigraphic time series at fixed locations, but we tried to choose a location as representative of the local snowpack as possible for each new pit. On occasion, dyed water was sprayed on the snow to accentuate vertical and horizontal flow paths. Density was measured using both snow water equivalent (SWE) tubes for coring as well as 100-cc cutters weighed to 0.1 g for pit layer densities.

Snow depths were measured every meter along a 200-m line located on the north edge of each swath (Figure 2 through Figure 5) using an automatic depth probe (Sturm & Holmgren, 2018). To ensure repeat locations, the lines were marked by tripods and stakes, and two 100-m tapes were stretched along the line to guide measurements. We measured these lines about 14 times each season. Over-probing and relocation uncertainty resulted in an absolute depth accuracy of about ±1.5 cm with a differential accuracy between two surveys of about ±2 cm. In practice, we frequently noted that the probe was inserted in the same hole in the snow from the previous day's survey, increasing the differential accuracy to better than ±1 cm.

Spectral albedo measurements were made using an ASD FieldSpec Standard-Res Spectroradiometer (https://www.malvernpanalytical.com/) as a function of wavelength from 350 to 2,500 nm. Forty-one measurements were made along each line at 5 m intervals concurrent with each set of snow depth measurements. Due to the need to preserve the snow for the ASD, those measurements were made about 1.5 m south of the depth line. Here we report the 500 and 1,000 nm results, which (Grenfell & Maykut, 1977; Mellor, 1965; Perovich, 2007) have been shown to be a good index for the broadband albedo in the visible and near-infrared wavelengths. Sky conditions in 2019 were recorded by a stationary upward-looking GoPro fisheye camera. In 2022, a stationary Kipp and Zonen albedometer was used.

Snow water equivalent (SWE) measurements were made adjacent to the larger swaths using a Federal corer. The cored snow was decanted into plastic bags and weighed to a precision of 0.1 g. As the melt progressed and the snowpack had more internal ice features and liquid water, the measurements became more difficult to obtain, due to the hardness of internal ice and difficulty preserving the liquid water content. We therefore supplemented cores with density measurements of individual layers integrated to produce bulk density values.

Table 2
Measurements With Corresponding Sampling Location, Number of Measurements, Sampling Frequency, and Instrument

Measurement	Location	*n*-value	Frequency	Instrument
Snow Depth	200-m line	201	Daily	Automatic depth probe
Spectral Albedo	200-m line	41	Daily	ASD
Oblique Photos	200-m line	>80	Daily	iPad
Aerial Oblique Photos (2019)	200 × 20 m swath	Hundreds	Daily	Go-Pro on 5-m pole (2019); DJI
Aerial Oblique Photos (2022)	500 × 500 m area	Hundreds	Daily	DJI RTK Phantom
Snow-Interface Temp. (2019) (BTS)	200-m post	~4,800 total	Every 15 min	Hobo Pro U23
Snow-Interface Temp. (2022)	Various	~20,000 total	Every 10 min	Hobo Pro U23
Air Temperature (2019 and 2022)	200-m post	~4,800 total	3 locations every 15 min	Hobo Pro U23
Snow Density and Temperature Layering and Wetness	Near 200-m lines off-swath	Several	Daily	See Int. Classification Snow on the Ground
Snow Grain Size Photos	Snow pits	Several	Daily	Olympus TG-5 camera
Snow Water Equivalent	Snow pits	10	Daily	Federal sampler
Radiation (SW and LW)	At NSA-ARM		Every minute	https://www.arm.gov/capabilities/observatories/nsa
Local Meteorology	At NSA-ARM		Every minute	https://www.arm.gov/capabilities/observatories/nsa

Note. If not otherwise specified, number of measurements is per period.

In addition to spot snow temperatures from snow pits, we installed BTS (Bottom Temperature Snow) sensors (Hiller et al., 2014) connected to data loggers (Onset Computers model U23). These were installed at the snow-substrate interface in April each year in snow of average depth at each site. The sensors provided a means of detecting the arrival of water near or at the base of the snow (Conway & Benedict, 1994; Sturm & Holmgren, 1993). We also installed local air temperature and humidity sensors that could be used to compare site-to-site differences in ambient conditions.

4.2. Aerial Imaging

Local regulations precluded drone flights in 2019, so orthomosaic maps of our swaths were produced using photos taken from the top of a 5-m pole (e.g., Visser et al., 2019). In 2022 we used an RTK-equipped DJI Phantom drone. Orthomosaic maps were generated using Agisoft Metashape Pro Version 1.7.2 (2021); these maps were draped over Digital Terrain Models (DTMs) to document melt patterns using structure-from-motion (SfM) photogrammetric techniques (Nolan et al., 2015). We generated binary images of snow/no-snow areas, the basis for computing snow cover fraction, using the Otsu method (Al-Rahlawee & Rahebi, 2021).

4.3. Computation of Melt Rates

There is no easy solution for determining melt rates in heterogeneous tundra snow, particularly if the goal is to produce a spatially distributed series of measurements. Coring and density sampling are destructive. Additionally, as the melt progresses and the snow becomes wet, it becomes difficult to core with precision. Since the melt is a mass conversion process, it can result in changes in both the depth, h, and density, ρ, of the snowpack. Per unit area, the rate of change of mass over time, t, is given by:

$$\frac{\partial(\rho h)}{\partial t} = \rho\frac{\partial h}{\partial t} + h\frac{\partial \rho}{\partial t} \tag{1}$$

assuming, that the dry density, ρ, is equal to the bulk density of the snow, as water retention in snow generally is very small (Avanzi et al., 2015; Bøggild, 2000). For snow on tundra and sea ice, the 2nd term on the right can often be ignored because both wind slab and depth hoar, the major components of that class (Sturm & Liston, 2021), are vertically "stiff" (Akitaya, 1974) with low densification rates (Sturm & Holmgren, 1998). In 2019, the total increase in bulk density, $\frac{\partial \rho}{\partial t}$, over most of the campaign was less than 9% ($n = 28$), hence negligible. There are limitations to this simplification when water remains in the snow, but in the end, practicality forced us to use depth measurements (the first term on the right-hand side of Equation 1) to explore the spatial variability in the melt, since we need n-values in the hundreds given the patchy nature of the snow (Clark et al., 2011).

To allow for site-to-site comparisons, we normalized the site-specific depth rates of change by a density scaling factor, defined as the ratio of the site average density (ρ_{site}) to the average snow density at ICE (ρ_{ICE}). Thus, neglecting densification and using Δ to designate finite differences derived from observations, Equation 1 can then be expressed as:

$$\frac{\Delta(\rho h)}{\Delta t} \approx (\rho) \cdot \left(\frac{\rho_{\text{site}}}{\rho_{\text{ICE}}}\right) \cdot \frac{\Delta h}{\Delta t} \tag{2}$$

In 2019, all three sites had nearly the same average density making the density scaling factor effectively 1; in 2022 the densities varied by less than 16% (Table 4). Depth-time data (typically 14 values) for each meter along the 200-m lines were fit with a linear model, the slope of which defined the depth-melt rate for the season at that probe position. We excluded the first occurrence of 0 cm of snow from the fitting procedure: (a) to avoid overestimating the time interval at which the snow disappeared (we did not always measure exactly the time at which the snow disappeared), and (b) this final value of ($\Delta h/\Delta t$) was often much larger than the other 13 values for various reasons including increasing light transmission through the thinnest (<2 cm) snow (Perovich, 2007) and maximum advected heat.

5. Results

5.1. Pre-Melt Snow Conditions

Snow usually arrives in Utqiaġvik in October and starts melting in mid-May (Stone et al., 2002; Weller & Holmgren, 1974). The area receives limited snowfall, but consistent winds above 6 m s^{-1} (Sturm & Stuefer, 2013). These winds transport snow and create snow bedforms such as drifts, dunes, and sastrugi (Filhol & Sturm, 2015).

Table 3
Pre-Melt Snow Conditions Measured 2019 and 2022

	2019 ARM	2019 BEO	2019 ICE	2022 ARM	2022 BEO	2022 ICE
Average depth (cm)	41.4	48.0	25.8	39.6	44.7	20.6
Standard deviation depth (cm)	15.6	10.4	8.5	9.5	8.9	6.5
Coefficient of variance	0.38	0.21	0.33	0.24	0.20	0.32
Maximum depth (cm)	93.9	83.0	49.8	82.8	62.7	41.4
Semivariogram range (m)	45.0	18.0	19.0	28.0	11.0	16.0

Note. Measurements taken every meter along each of the 200-m lines at the three sites.

Due to the proximity of the three sites to each other, snowfall and wind were similar and so were the snowpacks that developed (Tables 3 and 4). At ICE the SWE was less than at the other two sites because the sea ice did not form until November, after some snow had already accumulated on the tundra. At all the sites local bedforms ranged from 0.1 to 0.25 m high. At ICE, these were the sole factors driving depth variations because the sea ice substrate was nearly flat. At the tundra sites, with their more complex topography (Figures 3 and 4), the depth variability was the combined result of the tundra topography plus the bedform relief. On a larger scale at ARM, a prominent HCP at the east end of the line (Figure 3) produced a 40-m wide drift in both 2019 and 2022. It was large enough to create a snow depletion zone downwind (west) where the earliest exposure of bare tundra occurred in both melt years.

Statistically, within-site depth distributions were remarkably similar from 2019 to 2022 (Tables 3 and 4). We attribute this repeatability to the interaction of a reliable prevailing wind (predominantly from the northeast), frequently strong enough to re-distribute snow, interacting with the relatively fixed topography of tundra, or the absence of topography on level sea ice.

5.2. The Melt Sequences of 2019 and 2022

We can characterize the general melt progression for each year according to the average date of melt onset and the average duration of melt. To track these, we examine the air and BTS temperatures (Figures 6a and 6b), weather data from the NSA-ARM site, and detailed snow pit observations (Figure 7). To outline the general progression of the melt we followed Dingman's (2008) melt phases and divided the 2019 and 2022 melt accordingly (Figures 6a and 6b). However, this required some modifications of the phase definitions. Phase 1 in Dingman (2008) is described as "[…] the net input of energy to [the snowpack] becoming more or less continually positive until the entire pack is isothermal at 0°C." In thin, cold tundra snow, penetrative percolation of water reaches the base of the pack while large zones of snow remain as much as 10°C below freezing (Marsh & Woo, 1984a). Phase 1 overlaps Phase 2 (ripening), which is dominated by snow grain coarsening and more extensive percolation into the snow. We therefore used positive air temperatures accompanied by spikes in BTS temperatures, indicating the arrival of meltwater at the base of the snow, to mark the start of the melt and the beginning of Phase 2 (Conway &

Table 4
Pre-Melt Snow Conditions Based on Snow Pit Measurements, 2019 and 2022

	2019 ARM	2019 BEO	2019 ICE	2022 ARM	2022 BEO	2022 ICE
SWE (cm)	16.3	22.5	11.1	13.6	12.7	8.6
Average site density (kg/m3)	361	364	350	334	324	367
Density scaling factor	1.03	1.04	1.00	0.87	0.84	1.00
% depth hoar	59	40	31	63	53	61
% wind slab	40	52	50	33	43	32

Note. Measurements taken in snow pits away from the 200-m lines.

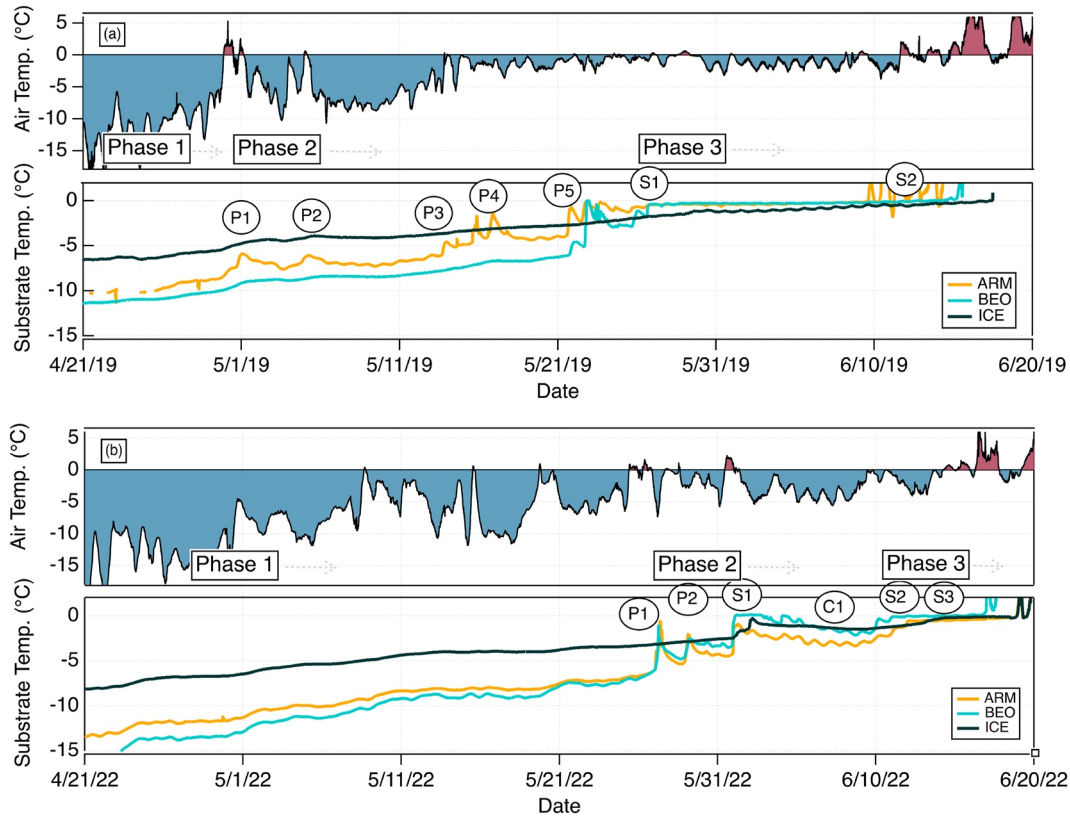

Figure 6. The melt sequences of 2019 (a) and 2022 (b). Air temperature is shown in the two upper panels and BTS (substrate temperatures) are shown in the lower panels. *P* indicates a percolation event; *S* indicates slush present; *C* indicates a cooling period when water at the base of the snow refroze. In 2019, water was infusing into the snowpack as early as 30 April, and the concentrated group of percolation events that occurred between 16 May and 24 May accelerated the melt. By 27 May standing water was ponding in some places under the snow, though this state was not detected at ICE until later. In contrast, percolation events did not begin until 27 May in 2022, yet slush was detected just 5 days later.

Benedict, 1994; Sturm & Holmgren, 1993). We marked the beginning of Phase 3 (the water output phase), which often overlaps Phases 1 and 2, when we observed water ponding or flowing beneath the snow. The snow turning fully isothermal and the BTS records consistently reporting 0°C is an indicator for that. We defined the end of the melt when about 95% of the snow (by area) was gone in our orthomosaic images (Figure 8a).

In 2019, air temperatures increased markedly on April 30th, and by the next day meltwater had percolated down to near the base of the snow marking the start of Phase 2 (Figure 6a, P1). After a short cold hiatus of melt on 5 May (P2), the same happened again briefly on 5 May (P2). A longer period of below-freezing temperatures followed, during which both basal and perched water froze in the pack, creating ice columns and lenses. On 14 May, when above-freezing temperatures returned, the percolation pipes seemed to have re-activated and there followed three more events of water percolating to near the base of the snow (P3-P5). By 29 May, after several days of consistent above-freezing temperatures, slush (S1) was finally detected at the base of the snow, indicating that whatever cold content had existed in the snow and substrate was now exhausted and Phase 3 had begun. At ICE, which had greater substrate cold content at this time in the melt, it was not until June 12th that basal slush was detected in snow pits and by the BTS sensors (S2). In all, in 2019 the melt progression took about 40 days, with the most intensive period of superimposed ice formation from 12 May to 23 May (Phase 2) (see Figure 7 for more detail).

In sharp contrast, the 2022 snowpack did not show meltwater percolating to the base until 27 May (Figure 6b, P1 and P2, start of Phase 2), with the first indications of slush and standing water at the base of the snow being recorded just 5 days later (S1, start of Phase 3). The melt progression was halted by a 6-day cold snap (C1), during which the BTS sensors indicated all basal water/slush had refrozen. Not until June 12th (by which time the melt at ARM had almost finished in 2019) did the melt of 2022 restart, but then it came on so fast that slush appeared at

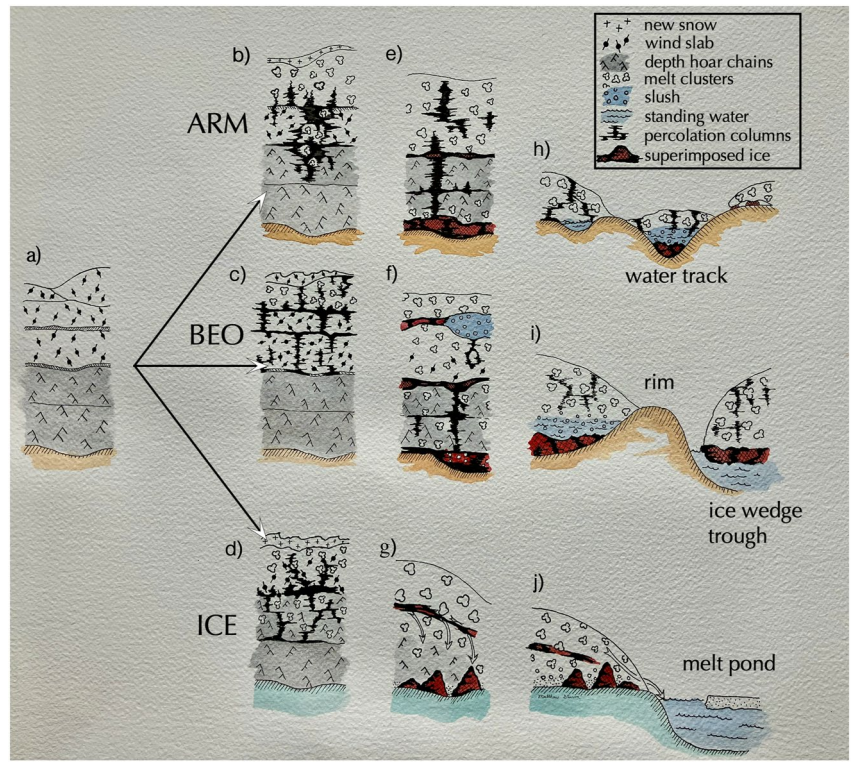

Figure 7. Snowmelt sequences from the three sites composited from 2019 to 2022 snow pit and trench observations, indicating internal and basal ice and slush features (see Fierz et al., 2009 for symbols). The three sites showed similar initial sequences (moderate surface grain coarsening, vertical percolation with lateral spreading at stratigraphic boundaries), but once water began to percolate to the base of the snow where it interacted with the substrate, significant differences arose.

the base of the snow at the same time (S2 and S3). The melt finished by 19 June, taking about 22 days, showing the same stages and start-and-stop behavior as 2019, but happening in half the time.

A more nuanced view of the melt sequence, particularly with respect to water, can be seen in the conceptual diagram depicting stratigraphic profiles of the three sites over the course of the melt season (Figure 7). The diagram is based on our observations of both the 2019 and 2022 melt seasons; however, we will follow the 2019 timeline in the following phase description.

Pre-melt phase 0

Phase 0 was similar at all three sites, with three distinct wind slabs overlying two depth hoar layers with some minor melt crusts (Figure 7a).

Phase 1 and Early Phase 2

While surface grain coarsening started in early May at all three sites (growth from 0.3 to 8 mm), meltwater only began draining downward in quantity, spreading laterally at the interfaces between wind slabs, and between wind slabs and depth hoar layers about a week after (Figures 7b–7d). At ICE, where the surface dunes were the most pronounced, we noticed a distinct down-slope movement of water away from higher dune centers.

Phase 2

By mid-May at ARM (Figure 7e) and about a week later at BEO (Figure 7f) and at ICE (Figure 7g), percolating water had reached the base of the snow and superimposed ice formation had begun. At ARM and BEO, the vegetated tundra soil started out with higher capacities to refreeze percolating meltwater due to the lower initial bulk temperatures (Figures 6a and 6b). However, as snowmelt progressed, the higher thermal conductivity and specific heat capacity of sea ice, coupled with bulk temperatures that remained lower for longer than those of tundra, the capacity to refreeze meltwater became higher for sea ice than tundra toward the end of phase 2.

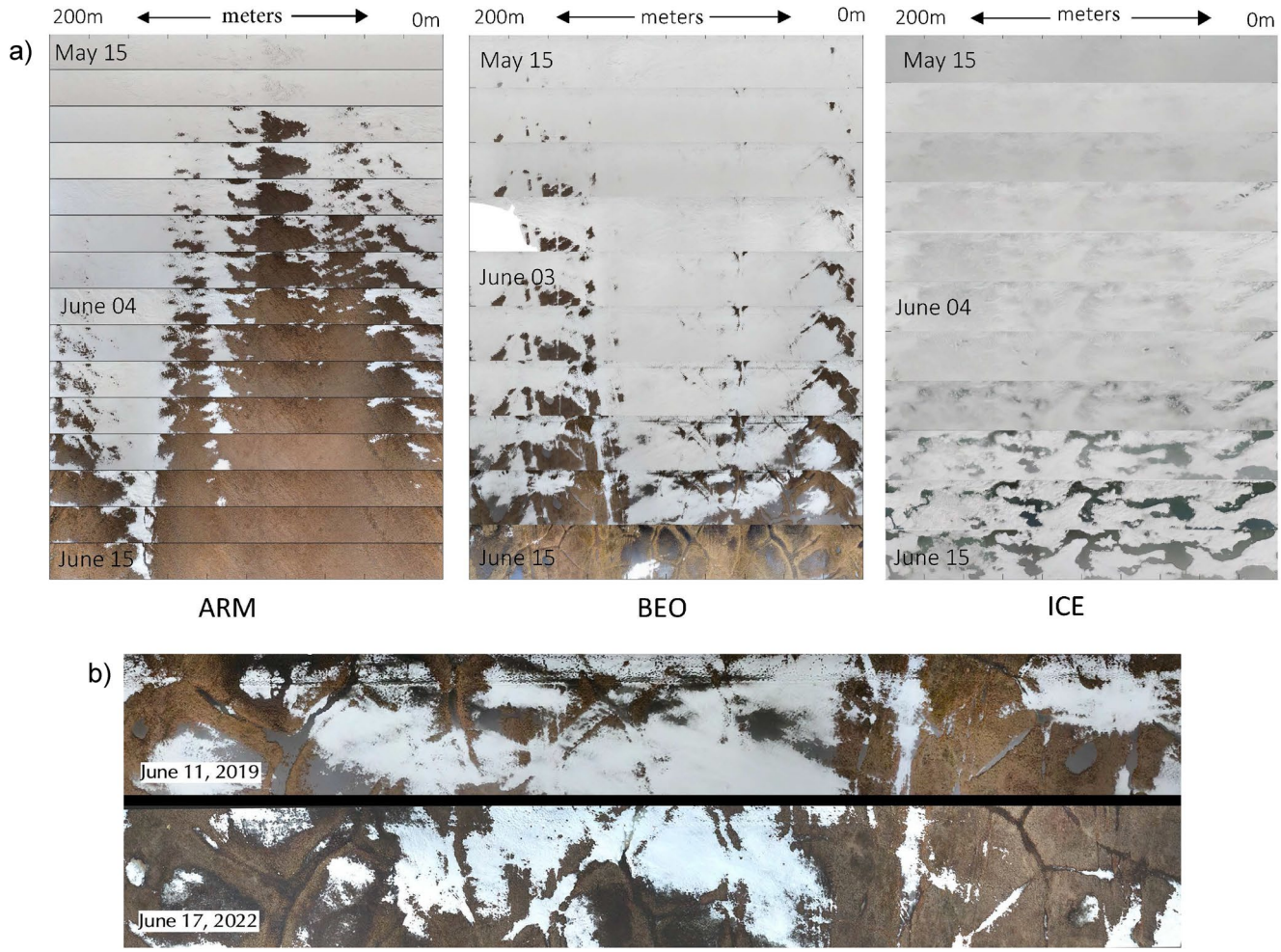

Figure 8. (a) Orthomosaic sequences for the three sites in 2019 showing locations of early and late meltout as well as ponded water and melt pond development (north is up). Note that at ICE, the gray areas which later turned to melt ponds can be seen as early as 20 May. (b) Meltout patterns at BEO, 2019 and 2022, showing their similarity in the 2 years. Repeat patterns in tundra snow have been documented by Sturm and Wagner (2010) and Parr et al. (2020) and have also been observed in maritime snow (Pflug & Lundquist, 2020).

Early Phase 3

By the last week of May, standing water and slush were starting to be noted at the base of snow pits at ARM and BEO. At ARM, with its water tracks and hillslope terrain (Figure 3), ponding was limited to small puddles between tussocks. Consequently, over much of the site, little superimposed ice developed (Figure 7h, left and center). At BEO, superimposed ice formation was more extensive in this phase of the melt. There, ponding was favored by the closed depressions associated with LCPs and the poor drainage of ice-wedge networks (Figures 4 and 7i). At ICE, the high capacity to refreeze meltwater at this stage led to the growth of conspicuous ice mounds (Woo et al., 1982) at the snow-ice interface, though standing water had yet to appear (Figure 7g).

Phase 3

A strong increase in the divergence of the melt behavior between sites occurred early in June. At ARM, with its efficient drainage system, much of the snowpack evolved into patches of well-drained, grain-coarsened melt clusters sitting on relatively dry tundra (Figure 7h, right). These patches tended to melt fast. Only within the water tracks at ARM did we find substantial amounts of superimposed ice and standing water (Figure 7h, left and center). At BEO (Figure 7i), where water ponding was more extensive, upward wicking of standing water created a widespread layer of slush up to 15 cm thick. With the influx of additional water to the base, we observed two different effects. In some places, the superimposed ice that had developed in Phase 2 remained frozen to the ground and suppressed the vegetation under it. In other locations, the ice separated and then floated upward, in

many cases carrying the snowpack up and preserving it from water inundation and erosion (Figure 7i, right). At ICE, it was during this time that melt ponds began to form (Figure 7j). Once they did, they served as sinks for meltwater from adjacent higher areas of snow and ice, mostly the remnants of dunes. Continued melting at this point deepened and eventually enlarged the ponds but did little to alter the higher dune areas, which lasted longer than snow at the tundra site. Pond development produced a highly differentiated landscape where melting was intense.

The final stages of Phase 3 showed extensive heterogeneity in snowpack conditions. Diachroneity by this time was extreme: by moving just a few meters one way or another, we could find bare ground, open water, or snow patches in Phases 1, 2, or 3.

5.3. Snowmelt Patterns

Diachroneity develops largely due to landscape controls; we observed strikingly different melt patterns or patchiness at the three sites (Figure 8a), even though the sites experienced much the same weather, had similar aspects, and had similar pre-melt snowpacks (Tables 3 and 4). These pattern differences indicate that overall, melt rates must have been different both between sites and within sites due (in addition to Phase 0 differences) to the local substrate topography. For example, in 2019, bare tundra began to emerge at ARM more than 16 days before it was seen at BEO and expanded more rapidly at ARM. By June, a 40% difference in snow cover fraction (ARM vs. BEO) had developed. Large swaths of ARM, especially the drained slope areas, were snow-free while only the rims of LCPs had melted out at BEO. At ICE, the orthophotos (Figure 8a) showed the first signs of melting as areas of "graying" of the snowpack. These appeared as early as 20 May in 2019. The graying suggests that small amounts of water were percolating down to the ice surface and seeping along it, for almost without exception, these gray areas became melt ponds later. A similar graying was observed in 2022. Pit observations (Figure 7), however, revealed no standing water. It took another 16 days before melt ponds had formed.

In 2022, the meltout patterns were not as strongly differentiated because of the compressed duration of the melt, but they still mirrored the 2019 patterns (Figure 8b) due to the strong landscape controls on Arctic snow distribution (Parr et al., 2020) and melt mechanisms.

5.4. Computation of Meltout Dates

The meltout patterns in Figure 8a suggest landscape-controlled melt rates, which are intertwined with meltout effects due to pre-melt snow depth variations (Cline et al., 1998; Guan et al., 2013; Liston, 1999). To separate the two effects, we employed a surface energy balance model (SnowModel, Liston & Elder, 2006), driving it with atmospheric input data from ARM-NSA. As the melt progressed, spatial variations in snow albedo along the three lines could have influenced the melt, with areas of lower albedo melting at accelerated rates. However, our albedo measurements in the visible (VIS, 500 nm) and the near-infrared range (NIR, 1,000 nm) show that, at both wavelengths, albedo values varied less than 15% as long as snow covered the ground, even when the snow was thin. Once the snow melted, however, visible albedo values between snow covered and snow free patches varied by up to 81% at ARM (NIR: 31%), 85% at BEO (NIR: 15%), and 68% at ICE (NIR: 34%).

Following the methods discussed by Luce et al. (1999) and Liston (2004), we have compared the modeled meltout dates for each meter along the measurement lines (using the initial measured snow depth) with the actual meltout dates (Figure 9). For graphical clarity, we smoothed the theoretical meltout date line (heavy black lines in Figure 9) using a three-pass binomial filter producing 3-m spatial averaging.

The results show that, while pre-melt depth was a control on meltout date, there were many places where landscape-driven melt mechanisms (including advected heat via water and wind) were at work, resulting in spatially heterogeneous melt rates at each site (see also Essery & Pomeroy, 2004; Faria et al., 2000; Pomeroy et al., 2001, 2003). We have marked a few of these in Figure 9 with "E"s and "L"s, denoting when actual melt occurred earlier or later than the modeled date, respectively. For example, at ARM at 68, 123, and 191 m, the snow in 2019 lasted more than a week longer than predicted by the melt model.

To further quantify these heterogeneous melt rates, we have plotted meltout date as a function of pre-melt depth and applied a linear fit for each site and year (lower panels, Figure 10). Under a uniform melt rate assumption, we would expect a very tight fit (high r^2-values) because pre-melt depth would explain all, or certainly most,

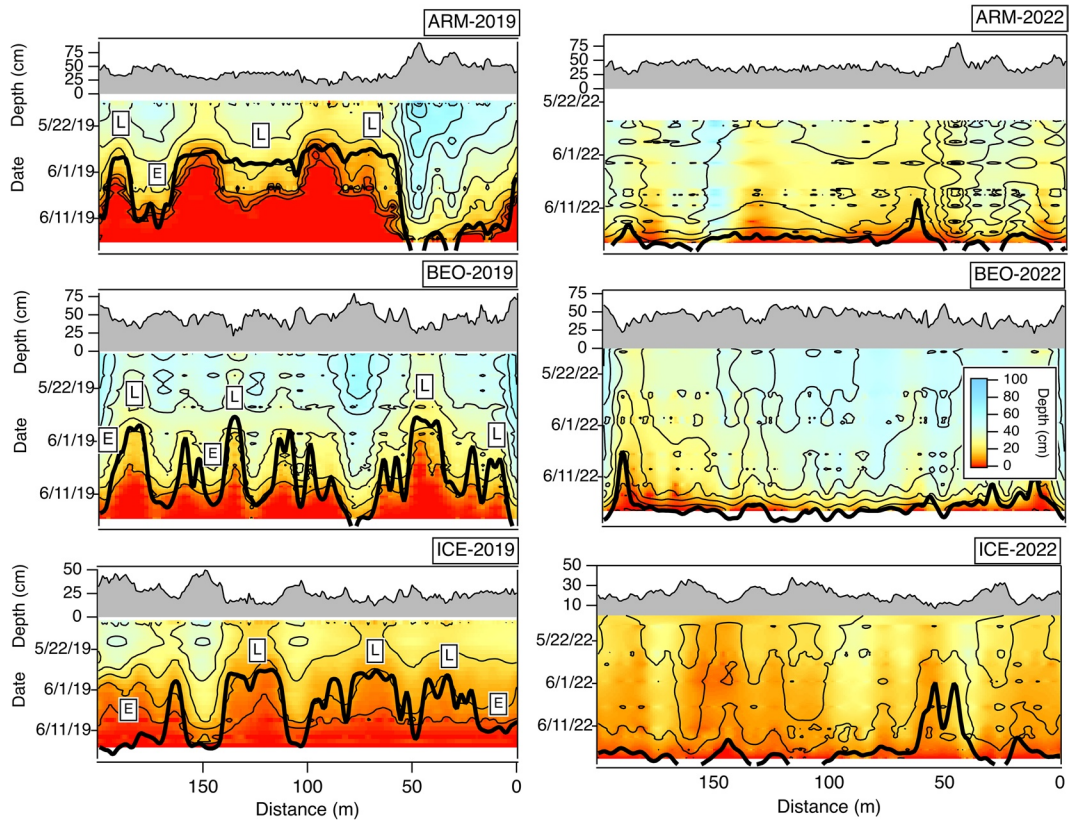

Figure 9. Meltout contour maps for the three sites in 2019 and 2022. The colored contour maps are derived from measurements made along the snow depth lines ($n = 201$) that were repeated ~14 times during each season. Those data have been contoured to make time-depth maps; red indicates "no snow." The top panel above each site map is the pre-melt snow depth profile (gray). The heavy black lines are theoretical meltout dates under a uniform melt rate assumption, computed using an energy balance model, forced by meteorological data from the nearby ARM-NSA research facility (ENBAL subroutine in SnowModel, Liston & Elder, 2006).

of the variation in the meltout date. However, the r^2-values listed in Figure 10 are relatively low, and pre-melt depths explain only 0.21 (ICE), 0.60 (BEO), and 0.72 (ARM) of the snow persistence at the sites in 2019, with r^2 values being lower in 2022. The residuals (top panels, Figure 10) show considerable scatter about the fit, in some cases as much as ±10 days compared to the expected value if pre-melt snow depth was the only control on meltout date. These findings indicate that melt mechanisms were operating at each site, speeding up or slowing the melt in specific locations. Another key finding is that the ensemble of melt mechanisms stayed relatively the same from 1 year to the next, indicating that the ensemble had a fixed geographic component arising from the site topography and substrate.

5.5. Albedo Evolution

As the melt season progressed through snow metamorphism and surface condition changes, we observed a similar spectral albedo evolution as Vérin et al. (2022), Grenfell and Perovich (2004), Perovich et al. (2002), namely a significant and early reduction in NIR albedo values (1,000 nm) during Phases 1 and 2 then a drastic drop in VIS albedo values (500 nm) in Phase 3. The reduction in NIR albedo values during Phases 1 and 2 accelerated snowmelt, but the values decreased quite homogenously (Section 5.4) so reductions in albedo values while the lines were still snow-covered are unlikely to have added to melt diachroneity.

The spatial variability was greatest in Phase 3 for both VIS and NIR values. However, the range of NIR albedo values was generally smaller, especially at the two tundra sites. The shift in spectral maxima (Grenfell & Perovich, 2004) due to coarsened grains and emerging tundra vegetation both lie around ~0.4. This is shown in Figure 11. We overlaid both VIS and NIR albedo values on the 4 June 2019 orthomosaic image of the ARM site.

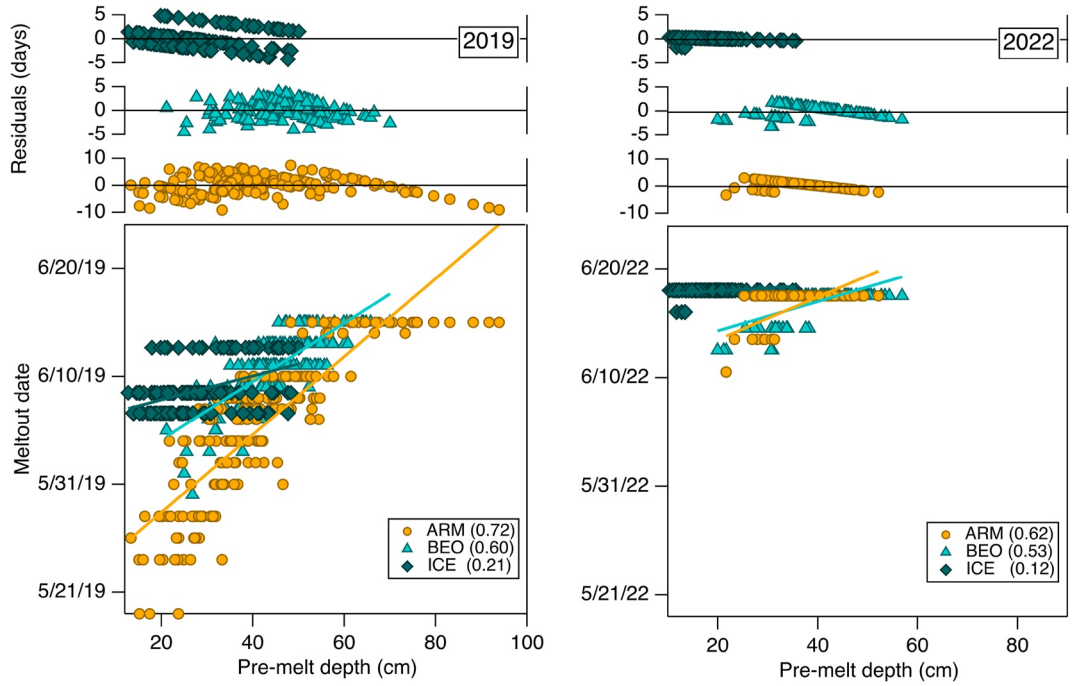

Figure 10. Bottom: Meltout date (no snow) as a function of pre-melt depth for the 3 sites in 2019 (left) and 2022 (right). The R^2 values to the linear fits are shown in a box in each panel. Top: The residuals of the linear models color-coded by site.

While VIS albedo values range from 0.81 to 0.93 in snow-covered areas, the bare tundra areas albedo values range from 0.08 to 0.16. Where the ASD picked up a mixture of bare and snow-covered ground, we recorded values of between 0.4 and 0.6. The NIR spectrum has a much smaller range of albedo values of 0.32–0.62. Snow-covered areas had a NIR albedo range of 0.54–0.62 while tundra locations ranged between 0.32 and 0.48. The meltout date thus is important climatologically as it marks the time of the most abrupt change in albedo.

5.6. Melt Mechanisms

5.6.1. Tundra

In classic energy balance modeling approaches, the only way to have spatially variable melt rates is to have spatially varying atmospheric forcing fields, but those differences were minimal in our experimental design. Nonetheless, as indicated in Figure 7 through Figure 10, considerable heterogeneity in melt rates and meltout dates were observed, so advective processes must have been at work enhancing melt in some locations, inhibiting it in others. As discussed above, turbulent latent and sensible heat was undoubtedly one such mechanism, but from the extensive photo archives taken during the melt of 2019 and 2022, we have identified 7 water-related advective mechanisms driven largely by the interaction of the local substrate and snow interacting with meltwater that were at play as well.

We identified three distinct mechanisms that enhance tundra melt, the first of which involves large quantities of flowing water eroding break-through channels through snow cover (Figure 12a). The second mechanism is the

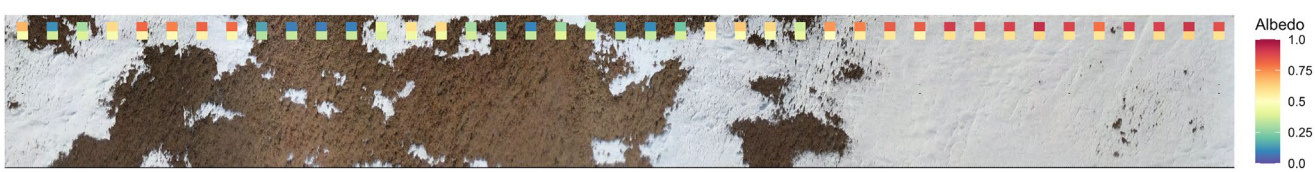

Figure 11. The visible (VIS, 500 nm—upper row) and near-infrared (NIR, 1,000 nm—lower row) albedo values taken on 4 June 2019 overlain on the orthomosaic image of the ARM site of the same day. The VIS albedo values show a greater range of albedo values from 0.93 to 0.08 than the NIR values which range from 0.62 to 0.32. Overall, the largest change in albedo was observed just before the respective melt out day for each snow patch.

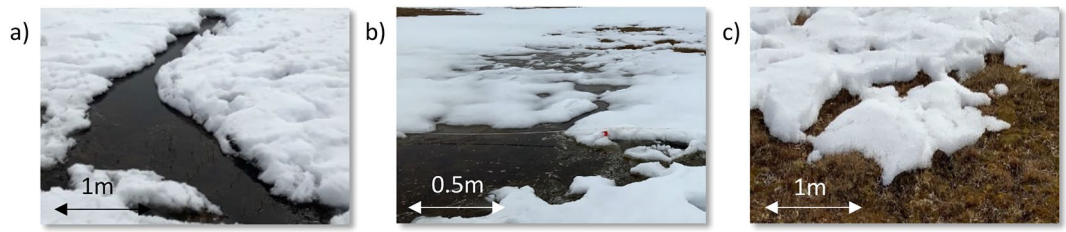

Figure 12. Three melt-enhancing mechanisms. (a) Break-through erosion channels in locations of concentrated water flow. Range: 1–30 m. (b) Water inundation that introduced advected heat in closed basins like LCPs. Range: <15 m. (c) Water that drained from perched snow, reducing internal ice refreezing. Range: <1 m.

inundation of snow patches by water, which transports sensible heat that can melt or warm surrounding snow (Figure 12b). Lastly, complete water drainage from snow patches limits internal ice formation and therefore reducing latent heat required for further melt.

Similarly, we identified four tundra melt inhibiting mechanisms. First, the separation of the snowpack from the underlying substrate prevents mechanical and thermal erosion by flowing water (Figure 13a). Second, the formation of buoyant of snow rafts, which holds the snow above water as ponding increases and helps maintain higher albedo (Figure 13b). Third, emplacement of an icy base under the snow with a higher albedo than the natural substrate material, which limits light transmission through to the dark base (Figure 13c). And fourth, the formation of icy basal snow (Figure 13d), which suppresses vegetation that would otherwise protrude through the snow and absorb solar energy (Sturm et al., 2005).

An additional mechanism, the latent heat buffer imposed when liquid water in and below the snowpack refreezes has been discussed in detail by Woo et al. (1982) and Marsh and Woo (1984a, 1984b), and recently has become important in the percolation zone of Greenland (MacFerrin et al., 2019).

5.6.2. Sea Ice

Melt outcomes on sea ice differed from those on tundra. By altering its topography through the melt, the ice develops a more segregated solar-absorbing versus solar-reflecting landscape, with most of the melt energy concentrated in the ponds. This segregation is aided by the fact that as the snow melts in non-pond areas, it exposes white granular ice rather than dark tundra. Once segregated, further melting deepens the ponds but the bright snow dunes adjacent to the ponds resist melting and remain until late into the melt. On sea ice, we also identified a number of distinct mechanisms responsible for enhancing and inhibiting snow melt, but they were different from the tundra-specific mechanisms described above.

The first of two sea ice-specific melt-enhancing mechanisms is the development of ponds in low areas adjacent to snow dunes, where water inundation melted and removed all snow, leading to some of the highest melt rates observed. The second such mechanism is pond break-out, where a melt pond is no longer able to accommodate the influx of meltwater and breaks through to an adjacent pond, eroding snow in its path.

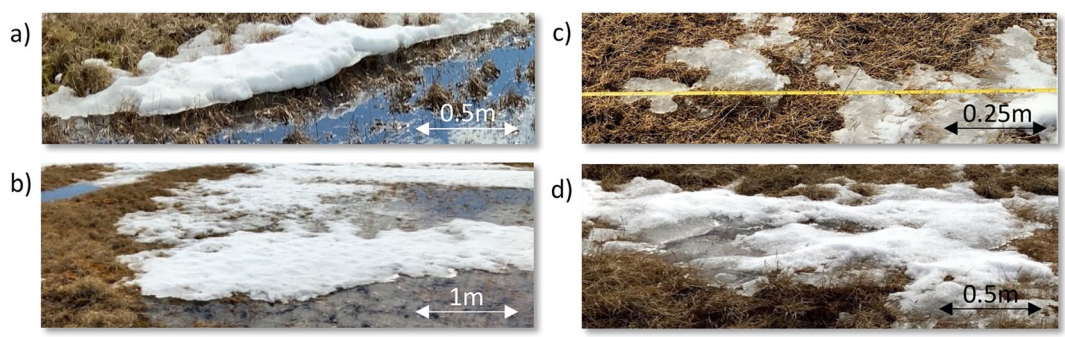

Figure 13. Four melt-inhabiting mechanisms. (a) Basal ice that separated snow from the substrate, preventing erosion by water. Range: 0.1–5 m. (b) Ice and snow that created floating rafts that lifted snow as ponded water increased. Range: 0.5–15 m. (c) Basal ice under snow that masked dark substrate limiting light transmission. Range: 0.1–1 m (d) Basal ice and icy snow that kept vegetation from protruding through the snow. Range: <1 m.

Our observations also revealed three mechanisms that inhibit snow melt on sea ice. First, the development of ice mounds under snow dunes creates a latent heat buffer slowing later melt. Second, surface ice, such as thin fringes of floating ice along the edges of ponds, prevent physical and thermal pond enlargement by wave action. Third, the same thin ice fringes, having a higher albedo than the dark water of the ponds, limiting the absorption of sunlight.

5.7. Linking Meltout Dates and Water-Related Melt Mechanisms

Ideally, we would like to be able to explicitly link water-snow melt mechanisms (Figures 12 and 13) with specific landscape locations and from that identify the specific reasons for enhanced or diminished melt rates observed, but that has proven to be difficult. As a start, we computed depth-melt rates at every meter of our lines for the 2019 data, with changes in depth scaled by the density scaling factors in Table 3 (see Section 5.1). These depth-melt rates have been plotted as a function of pre-melt depth in Figure 14a, each datum color-coded by its location along the measurement line. To make the connection to landscape features, we then overlaid the same data (now color-coded by depth melt rate) on snow-free orthophotos from the sites (Figure 14b).

The plots in Figure 14a show very different site-to-site melt rates and behaviors. Site-averaged rates were about 1.5 times higher on the tundra than on the sea ice (Table 5) despite similar atmospheric conditions, demonstrating that local mechanisms were also at work. The scatter in the data for each site suggests that the ensemble of such mechanisms differed by site. The structure of the scatter, broadly, can be explained by landscape and substrate controls. At ARM, a thin pre-melt depletion zone of about 20 cm downwind of a large drift, likely generated the five-fold range of melt rates where there was almost no control by pre-melt depth. Figure 14b shows that small drainage channels on the sloped, western part of the swath could have led to the variation in these melt rates. Over the rest of the swath, a strong relationship between melt rate and pre-melt existed. At BEO, the trend of increasing melt rate with pre-melt depth was stronger, but there was no obvious section of the line where preferentially high or low melt rates occurred due to the shorter structural length of the BEO landscape features. At ICE, pre-melt depth was a far better predictor of melt rate than at either tundra site, as reflected in an r^2 value of 0.65, yet the site-averaged melt rate was the lowest. In addition, at ICE, the scatter in the data was far more structured than at the other sites, mostly due to melt pond formation. At all sites, the within-site range of melt rates (Table 5, values in parentheses) was notably large, a strong indication of variations in melt rates at scales of tens of meters or less.

Melt rates for deeper snow are higher than for shallow snow. In part, because the time span of the melt for deeper snowpacks is longer, at those locations the melt extends later into spring, a time of greater solar insolation. In addition, the greater availability of lateral energy transfers later in the melt, sourced from shallow snow areas that have melted out early, also increase melt rates of at thicker snow patches.

6. Discussion

In this re-examination of Arctic snowmelt, we describe a system in which the most rapid reductions in albedo occur during Dingman's melt Phases 2 and 3 when water-driven melt mechanisms (Figures 12 and 13) and lateral turbulent heat fluxes predominate. As both mechanisms advect heat laterally, they produce complex, spatially heterogenous meltout patterns on both tundra and sea ice (Figures 8a and 8b). These mechanisms, especially water melt mechanisms, are tightly coupled to landscape features and thus lead to similar meltout patterns appearing each year. Combined with heterogeneous pre-melt snow distributions, these mechanisms can result in large variations in meltout dates (several weeks) and spatial variable melt rates (Table 5) that cannot be explained by pre-melt snow variations alone. Fundamentally, the nature of this Arctic melt system is *diachronous*, with individual patches of tundra or sea ice moving through melt phases at different timelines because multiple mechanisms are affecting the outcome.

Both systems, atmospherically driven and landscape-driven, overlap and operate simultaneously, raising the question of how to best combine the two in modeling. How should we account for the melt mechanisms and the melt heterogeneity they produce? And is it worth doing so?

The most common attempt to represent the complex evolution of snowmelt across a landscape is using depletion curves (COE, 1956; Essery & Pomeroy, 2004; Liston, 2004; Luce & Tarboton, 2004; Luce et al., 1999; Sexstone et al., 2020). Depletion curves are statistical depictions of the evolution of landscapes from their snow-covered

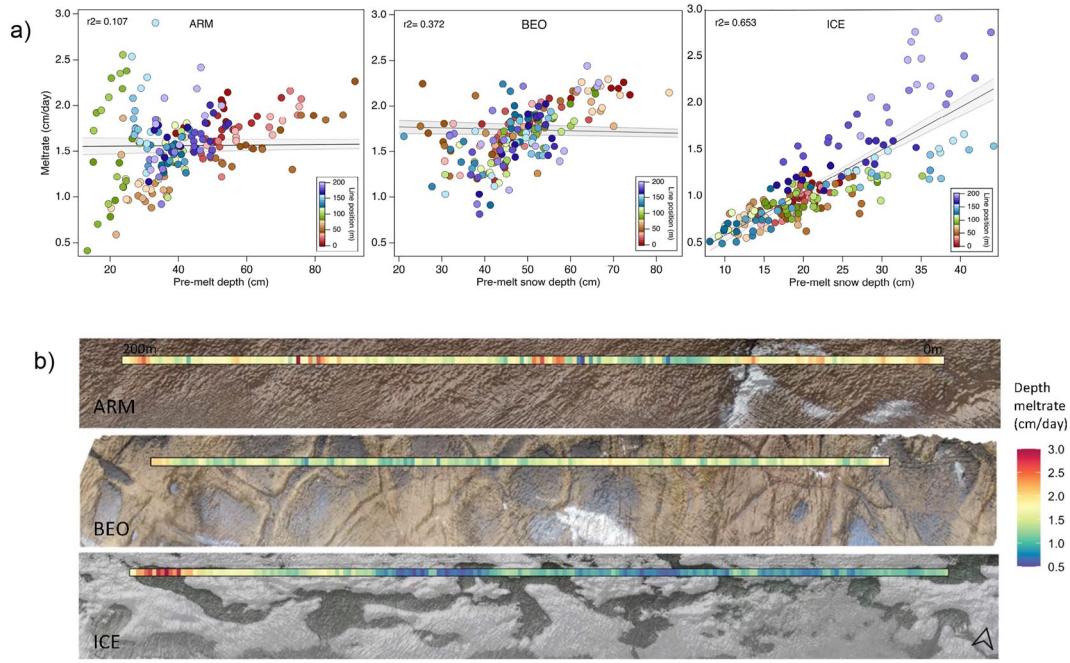

Figure 14. (a) Depth melt rates along the 200-m line in 2019 at each site as a function of pre-melt snow depth. The color of the circles indicates the location (m) along the line, the black line is a least-squares fit to the data, and the gray band is the 95% confidence interval. (b) Depth melt rates along the 200-m lines in 2019 for ARM (top), BEO (center), and ICE (bottom) overlain on the snow-free tundra orthomosaics taken on 17 June 2019 and the last orthomosaic we created for the 2019 melt season at ICE on 16 June 2019.

to their snow-free state as a function of the initial snow distribution. Clark et al. (2011), citing the work of Luce et al. (1999) and Liston (2004), present a thorough discussion of how depletion curves have been used to represent the sub-grid variability in snowmelt. They emphasize using the coefficient of variation (CV) of the pre-melt snow depth distribution to parameterize the curves. However, it is unclear whether this approach can account for the advective mechanisms that enhance or inhibit melt as described above. Our observations show that rather than being statistical, these mechanisms are physically mediated by substrate topography and conditions. The 2019 depletion curves from our three sites (Figure 15) bracket the two end-member depletion curves that are generally observed: (a) The curve for ARM shows a gradual linear reduction in snow-cover area as would be expected for a heterogeneous pre-melt snow distribution. The heterogeneity means there is a wide distribution of pre-melt depths, hence a slow and steady exposure of the substrate under the snow. (b) The curves for BEO and ICE remain high (near 100% snow cover fraction) much longer, then abruptly decline toward the end of the melt season. They are non-linear in nature, indicating a more homogeneous pre-melt snow distribution. Yet the CVs for the three sites (Tables 3 and 4) are so similar that they cannot explain why the curves differ. We would suggest that the differences, in part, arise due to the snow-water melt mechanisms described here, controlled by the substrate differences depicted in Figure 3 through Figure 5.

Table 5
Average Snow Depth-Melt Rates and Range of Melt Rates (cm/day) by Site in 2019 As Well As Average Pre-Melt (Snow Density Based) Mass Melt Rates and Range of Mass Melt Rates (kg/m²/day)

	Average melt rate		Range of melt rates	
Site	(cm/day)	(kg/m²/day)	(cm/day)	(kg/m²/day)
ARM	1.58	5.70	0.4–2.9 (7X)	1.4–10.5
BEO	1.69	6.15	0.8–2.5 (3X)	2.9–9.1
ICE	1.11	3.89	0.5–2.9 (6X)	1.8–10.2

How best to incorporate landscape-driven melt mechanisms into modeling approaches remains an open question. There are new approaches related to snowmelt run-off that perhaps hold promise, particularly those related to fill-and-spill (F + S) hillslope processes. McDonnell et al. (2021) provide a summary of the current thinking about F + S, and Spence and Woo (2003) and Coles and McDonnell (2018) have reported on F + S in snowy basins. In a general sense, the concept of F + S refers to the idea that a part of the landscape retains incoming water until a certain storage threshold is met, after which it is released. F + S processes arise from water-substrate interactions to produce highly non-linear responses in hillslope run-off. All the topographic elements needed for F + S were present in our study. We note that the snowpack itself is effectively an F + S aquifer (Webb et al., 2020) in

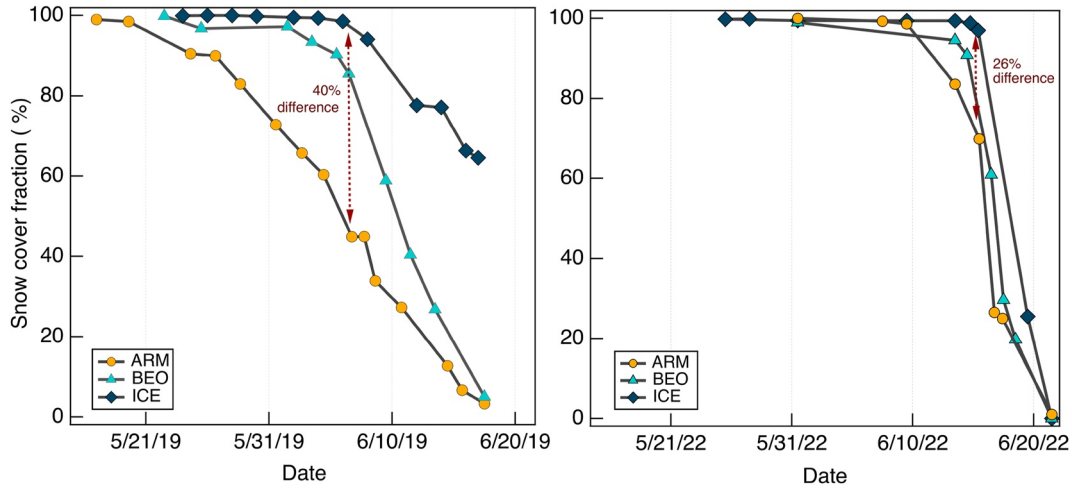

Figure 15. Depletion curves for ARM, BEO, and ICE derived from the photomosaics like that in Figure 8. Essery and Pomeroy (2004) have discussed that the greater the heterogeneity of the pre-melt snow distribution, the more linear the depletion curve.

which water can pond above internal ice layers and lenses (Figure 8), can be held in the snowpack pore spaces through capillary action, or can be released and drain away.

But is it worth worrying about all this small-scale, sub-grid melt variability? From a local standpoint, it might be. A key logistical challenge in the Arctic with little permanent infrastructure is transportation, for Arctic residents and industry alike. Understanding meltout patterns yields useful information for planning personal and commercial transportation routes.

From an energetics standpoint, it might be, too. In Figure 15, the 2019 depletion curves begin to diverge on 19 May 2019, when the curve for ARM drops rapidly while the BEO and ICE curves remain high, despite little atmospheric forcing difference between ARM and the other sites. The change in slope occurs at just about the time that the various melt-enhancing mechanisms were becoming prevalent. By June 1, the difference in snow-cover area between ARM and the other two sites was 40% (ARM-ICE) and 36% (ARM-BEO), implying a significant reduction in overall albedo at ARM. It was not until June 7 that the depletion curve of BEO began to drop. Using the difference between these areal curves, an assumed tundra albedo of 0.15, and a simple model of solar absorption for 70°N, we estimate that over the 30-day melt season, the enhanced melt at ARM produced an excess of energy of ~0.3 GJ/m^2. This difference in absorbed energy represents about a 12% increase in total annual heating of the ARM versus the BEO site. Considering the vastness of Arctic tundra and sea ice landscapes, it is worthwhile to understand the effect melt mechanisms have on the *timing* and the *rate* at which the albedo of a certain landscape type decays. Considering that Utqiaġvik receives one-third of its entire annual solar heating due to the approaching solstice between 15 May and 15 June, the key period in which we observed Arctic snowmelt, one can readily understand the climate implications melt diachroneity can have locally and globally (Grenfell & Perovich, 2004).

In 2022 (Figure 15, right), the melt season was compressed. Only a 26% difference in the snow-cover area developed between ARM and ICE and a 14% difference between ARM and BEO. This divergence in snow-covered area was maintained for less than 7 days, producing a smaller energetic difference between sites. Whether the ensemble of melt processes detailed in this study matters for the climate seems, therefore, in part, also to depend on which melt style (longer and slower vs. shorter and faster) is likely to be prevalent in a future, warmer Arctic climate. Earlier onset melt appears to lead to a more prolonged meltout season, encouraging advective melt mechanisms that produce large differences in snowmelt patterns and overall energy absorbed. Under this scenario, landscape mechanisms producing meltout heterogeneity take on increased importance. According to Stone et al. (2002), it is precisely this scenario we are likely to experience more often in the future.

7. Conclusions

We tracked the progression of snowmelt at three Arctic sites (two on tundra and one on landfast sea ice) over the course of two melt seasons in 2019 and 2022, focusing on the different water-related melt mechanisms underway.

In general, mechanisms that promoted water ponding tended to slow down the melt, while mechanisms that drained away water sped up the melt. We found that these mechanisms strongly increased melt diachroneity—enhancing, inhibiting, or even reversing the progression through the melt phases described in Dingman (2008) on a local, snow-patch scale.

For example, with increasing temperatures in spring, a snow patch on a rim of an LCP begins to melt and transitions through the Dingman melt phases rather quickly. Snow depths on polygon rims tend to be shallower and we observed the melt to be enhanced due to water draining away laterally (tundra enhancing mechanism [c]). Adjacent, lower-lying snow patches in the depressions of LCPs or the troughs to neighboring LCPs are the receivers of the laterally advected water sourced on the polygon rims. In topographic depressions, the snow tends to be deeper and the introduction of heat through water inundating the snow (tundra enhancing mechanism [b]) leads to a rapidly increased transition of these snow patches from a pre-melt condition (Phase 0) to the warming (Phase 1) and ripening (Phase 2) phase. As the arrival of water might occur during a time when the bulk substrate temperature of the tundra underneath the LCP depressions is still low enough to refreeze meltwater, superimposed ice can form. This triggers a release of latent heat to the surrounding snow and underlying substrate, driving the ripening of the snow patch further, however, it also adds to the cold content of the snow patch. As more meltwater pools in the depression, the superimposed ice detaches from the ground, floats to the surface of the forming pond, and preserves the overlying snow patch from melting (tundra inhibiting mechanism [b]), delaying the melt progression and retaining the snow patch in phase 2 for longer.

Water-related advection of heat is just one process that contributes to the diachroneity of melt at local scales and thus the creation of diverse Arctic snowmelt landscapes. Pre-melt variability in snow conditions is important (Liston, 1999), as is wind-driven advection of heat between different surface types that emerge during the later stages of melt. However, the recurrence of similar meltout patterns in different years suggests that it is the here-described nature of snow-meltwater interactions, which allow the substrate with its unique topography and composition to play a key role in this process. Our observations show, that during all phases of the melt, water plays a key role; Early in the melt, meltwater processes are important in establishing the meltout heterogeneity that follows later as it interacts with the topography before the substrate is exposed. Later in the melt, horizontal transport of heat and mass by meltwater running and ponding under and between snow patches may be the mechanisms by which substrate can shape the variety of meltout patterns we observed, especially as wind- and water-driven mechanisms start influencing each other more strongly.

We documented that the greatest reduction in albedo occurred in Phases 2 and 3, the wettest phases, and within a few days of the complete meltout of the snow. In 2019, as much as 25 days separated the first and last meltout patches at our sites, with a difference in snow-covered area of up to 40%. A difference of such magnitude during a time when solar radiation approaches its maximum in the Arctic can (theoretically) represent an additional 12% in annual solar heating, especially when weather conditions lead to an early onset and a prolonged duration of the melt season. The melt mechanisms we detail here drive changes in meltout patterns in the Arctic, therefore, are important to the climate.

Data Availability Statement

Data acquired during the field studies presented in this paper are available from the Department of Energy ARM archive (2019 link: https://www.arm.gov/research/campaigns/nsa2019salvo; 2022 link: https://www.arm.gov/research/campaigns/nsa2022salvoii; https://www.arm.gov/data/). ARM welcomes data users from all institutions and nations. A free ARM user account is needed to access ARM data. The energy balance model used in this paper (ENBAL) is part of the SnowModel system, which is described in detail by Liston and Elder (2006). The Fortran code for SnowModel, including the ENBAL module, is available at https://github.com/jupflug/SnowModel.

Acknowledgments

Many people helped with this project. Dr. Don Perovich provided advice on measuring albedo. Hannah Chapman-Dutton, Dr. David Clemens-Sewall, Trevor Grams, Owen Larson, Ema Mayo, Dr. David Shean, Dr. Melinda Webster, Serina Wesen, and Phillip Wilson assisted in the field. The U.S. Army Cold Regions Laboratory supplied our spectral radiometer. Dr. Glen Liston was generous in helping to implement ENBAL. Phillip Wilson conducted the Agisoft Metashape analysis, and Dr. Melinda Webster provided insight into melt pond behavior. Duncan Green and Dr. Julia Gestrich assisted with the statistics of snowmelt. We thank Dr. Ryan Webb for his insightful comments on an earlier draft of this paper, and the anonymous reviewers who pushed us to make the work more concise and accessible. This research was supported by the U.S. Department of Energy's Atmospheric System Research, an Office of Science Biological and Environmental Research program, under Grant DE-SC0019107. This research was also supported by the Atmospheric Radiation Measurement (ARM) User Facility, a U.S DoE Office of Science User Facility managed by the Biological and Environmental Research Program. The ARM NSA site operations team of Jimmy Ivanoff, Josh Ivanoff, Walter Brower, Valerie Sparks, Fred Heisel, Justin LaPierre, Ben Bishop, and Mark Ivey were of great assistance during the measurement seasons. Additional data were also obtained from the Atmospheric Radiation Measurement (ARM) User Facility archive. Logistical support was further provided by UIC Science, a subsidiary of the Ukpeaġvik Iñupiat Corporation (UIC), the Alaska Native Corporation representing shareholders from the community of Utqiaġvik, Alaska. Our field sites are located on the ancestral lands of the Iñupiat. We thank the Iñupiat for their stewardship and appreciate that we could work there.

References

Agisoft Metashape Pro Version 1.7.2. (2021). Downloads. Agisoft Metashape 1.7.2. Retrieved from https://www.agisoft.com/downloads/installer/

Akitaya, E. (1974). *Studies on depth hoar* (Vol. A26, pp. 1–67). Contributions from the Institute of Low Temperature Science.

Al-Rahlawee, A. T. H., & Rahebi, J. (2021). Multilevel thresholding of images with improved Otsu thresholding by black widow optimization algorithm. *Multimedia Tools and Applications*, *80*(18), 28217–28243. https://doi.org/10.1007/s11042-021-10860-w

Avanzi, F., Yamaguchi, S., Hirashima, H., & De Michele, C. (2015). Bulk volumetric liquid water content in a seasonal snowpack: Modeling its dynamics in different climatic conditions. *Advances in Water Resources*, *86*(Part A), 1–13. https://doi.org/10.1016/j.advwatres.2015.09.021

Benson, C. S. (1960). *Stratigraphic studies in the snow and firn of the Greenland ice sheet*. Research Report 70. Cold Regions Research and Engineering Laboratory.
Bøggild, C. E. (2000). Preferential flow and melt water retention in cold snow packs in west-Greenland. *Nordic Hydrology*, *31*(4/5), 287–300. https://doi.org/10.2166/nh.2000.0017
Callaghan, T. V., Johansson, M., Brown, R. D., Groisman, P. Y., Labba, N., Radionov, V., et al. (2011). The changing face of Arctic snow cover: A synthesis of observed and projected changes. *Ambio*, *40*(1), 17–31. https://doi.org/10.1007/s13280-011-0212-y
Clark, M. P., Hendrikx, J., Slater, A. G., Kavetski, D., Anderson, B., Cullen, N. J., et al. (2011). Representing spatial variability of snow water equivalent in hydrologic and land-surface models: A review. *Water Resources Research*, *47*(7), W07539. https://doi.org/10.1029/2011WR010745
Cline, D. W., Bales, R. C., & Dozier, J. (1998). Estimating the spatial distribution of snow in mountain basins using remote sensing and energy balance modeling. *Water Resources Research*, *34*(5), 1275–1285. https://doi.org/10.1029/97WR03755
COE. (1956). *U.S. Army corps of engineers, snow hydrology: Summary report of the snow investigations*. U.S. Army of Engineers North Pacific Division.
Coles, A. E., & McDonnell, J. J. (2018). Fill and spill drives runoff connectivity over frozen ground. *Journal of Hydrology*, *558*, 115–128. https://doi.org/10.1016/j.jhydrol.2018.01.016
Colombo, R., Garzonio, R., Di Mauro, B., Dumont, M., Tuzet, F., Cogliati, S., et al. (2019). Introducing thermal inertia for monitoring snowmelt processes with remote sensing. *Geophysical Research Letters*, *46*(8), 4308–4319. https://doi.org/10.1029/2019GL082193
Conway, H., & Benedict, R. (1994). Infiltration of water into snow. *Water Resources Research*, *30*(3), 641–649. https://doi.org/10.1016/j.jhydrol.2018.01.016
Curry, J. A., Schramm, J. L., & Ebert, E. E. (1995). Sea ice-albedo climate feedback mechanism. *Journal of Climate*, *8*(2), 240–247. https://doi.org/10.1175/1520-0442(1995)008<0240:siacfm>2.0.co;2
Dingman, S. L. (2008). *Physical hydrology, (reissued)*. Waveland Press Inc.
Doherty, S. J., Grenfell, T. C., Forsström, S., Hegg, D. L., Brandt, R. E., & Warren, S. G. (2013). Observed vertical redistribution of black carbon and other insoluble light-absorbing particles in melting snow. *Journal of Geophysical Research: Atmospheres*, *118*(11), 5553–5569. https://doi.org/10.1002/jgrd.50235
Domine, F., Barrere, M., & Sarrazin, D. (2016). Seasonal evolution of the effective thermal conductivity of the snow and the soil in high Arctic herb tundra at Bylot Island, Canada. *The Cryosphere*, *10*(6), 2573–2588. https://doi.org/10.5194/tc-10-2573-2016
Eicken, H. (1994). Structure of under-ice melt ponds in the central Arctic and their effect on, the sea-ice cover. *Limnology & Oceanography*, *39*(3), 682–693. https://doi.org/10.4319/lo.1994.39.3.0682
Essery, R., & Pomeroy, J. (2004). Implications of spatial distributions of snow mass and melt rate for snow-cover depletion: Theoretical considerations. *Annals of Glaciology*, *38*, 261–265. https://doi.org/10.3189/172756404781815275
Faria, D. A., Pomeroy, J. W., & Essery, R. L. H. (2000). Effect of covariance between ablation and snow water equivalent on depletion of snow-covered area in a forest. *Hydrological Processes*, *14*(15), 2683–2695. https://doi.org/10.1002/1099-1085(20001030)14:15<2683::AID-HYP86>3.0.CO;2-N
Farquharson, L. M., Mann, D. H., Grosse, G., Jones, B. M., & Romanovsky, V. E. (2016). Spatial distribution of thermokarst terrain in Arctic Alaska. *Geomorphology*, *273*, 116–133. https://doi.org/10.1016/j.geomorph.2016.08.007
Fierz, C., Armstrong, R. L., Durand, Y., Etchevers, P., Greene, E., McClung, D. M., et al. (2009). *The international classification for seasonal snow on the ground. IHP-VII technical documents in hydrology, 83, IACS contribution N°1*. UNESCO-IHP.
Filhol, S., & Sturm, M. (2015). Snow bedforms: A review, new data, and a formation model. *Journal of Geophysical Research: Earth Surface*, *120*(9), 1645–1669. https://doi.org/10.1002/2015JF003529
Frost, G. V., Christopherson, T., Jorgenson, M. T., Liljedahl, A. K., Macander, M. J., Walker, D. A., & Wells, A. F. (2018). Regional patterns and asynchronous onset of ice-wedge degradation since the mid-20th century in Arctic Alaska. *Remote Sensing*, *10*(8), 1312. https://doi.org/10.3390/RS10081312
Gold, R. D., Cowgill, E., Arrowsmith, J. R., Gosse, J., Chen, X., & Wang, X.-F. (2009). Riser diachroneity, lateral erosion, and uncertainty in rates of strike-slip faulting: A case study from Tuzidun along the Altyn Tagh Fault, NW China. *Journal of Geophysical Research*, *114*(B4), B04401. https://doi.org/10.1029/2008JB005913
Grenfell, T. C., & Maykut, G. A. (1977). The optical properties of ice and snow in the Arctic Basin. *Journal of Glaciology*, *18*(80), 445–463. https://doi.org/10.3189/S0022143000021122
Grenfell, T. C., & Perovich, D. K. (2004). Seasonal and spatial evolution of albedo in a snow-ice-land-ocean environment. *Journal of Geophysical Research*, *109*(1), C01001. https://doi.org/10.1029/2003jc001866
Guan, B., Molotch, N. P., Waliser, D. E., Jepsen, S. M., Painter, T. H., & Dozier, J. (2013). Snow water equivalent in the Sierra Nevada: Blending snow sensor observations with snowmelt model simulations. *Water Resources Research*, *49*(8), 5029–5046. https://doi.org/10.1002/wrcr.20387
Hanson, K. J. (1961). The albedo of sea ice and ice islands in the Arctic Ocean basin. *Arctic, Journal of the Arctic Institute of North America*, *14*(3), 188–196. https://doi.org/10.14430/arctic3673
Harder, P., Pomeroy, J. W., & Helgason, W. D. (2019). A simple model for local-scale sensible and latent heat advection contributions to snowmelt. *Hydrology and Earth System Sciences*, *23*, 1–17. https://doi.org/10.5194/hess-23-1-2019
Hiller, C., Keuschnig, M., Hartmeyer, I., & Götz, J. (2014). Assessment of the temperature variability at the snow-ground interface-concept and first results. In *EGU general assembly conference abstracts (14882)*.
Jost, G., Moore, R. D., Smith, R., & Gluns, D. R. (2012). Distributed temperature-index snowmelt modelling for forested catchments. *Journal of Hydrology*, *420–421*, 87–101. https://doi.org/10.1016/j.jhydrol.2011.11.045
König, M., & Sturm, M. (1998). Mapping snow distribution in the Alaskan Arctic using aerial photography and topographic relationships. *Water Resources Research*, *34*(12), 3471–3483. https://doi.org/10.1029/98WR02514
Lam, A. R., Crundwell, M. P., Leckie, R. M., Albanese, J., & Uzel, J. P. (2022). Diachroneity rules the mid-latitudes: A test case using Late Neogene planktic foraminifera across the western Pacific. *Geosciences*, *12*(5), 190. https://doi.org/10.3390/geosciences12050190
Lara, M. J., McGuire, A., Euskirchen, E. S., Tweedie, C. E., Hinkel, K. M., Skurikhin, A. N., et al. (2015). Polygonal tundra geomorphological change in response to warming alters future CO_2 and CH_4 flux on the Barrow Peninsula. *Global Change Biology*, *21*(4), 1634–1651. https://doi.org/10.1111/gcb.12757
Lara, M. J., Nitze, I., Grosse, G., Martin, P., & McGuire, A. D. (2018). Reduced arctic tundra productivity linked with landform and climate change interactions. *Nature Scientific Reports*, *8*(1), 2345. https://doi.org/10.1038/s41598-018-20692-8
Lidar Datasets at NOAA Digital Coast. (2019). AK DGGS Lidar. Retrieved from https://coast.noaa.gov/htdata/lidar1_z/
Liston, G. E. (1995). Local advection of momentum, heat, and moisture during the melt of patchy snow covers. *Journal of Applied Meteorology and Climatology*, *34*(7), 1705–1715. https://doi.org/10.1175/1520-0450-34.7.1705

Liston, G. E. (1999). Interrelationships among snow distribution, snowmelt, and snow cover depletion: Implications for atmospheric, hydrologic, and ecologic modeling. *Journal of Applied Meteorology and Climatology*, *38*(10), 1474–1487. https://doi.org/10.1175/1520-0450(1999)038<1474:IASDSA>2.0.CO;2

Liston, G. E. (2004). Representing subgrid snow cover heterogeneities in regional and global models. *Journal of Climate*, *17*(6), 1381–1397. https://doi.org/10.1175/1520-0442(2004)017<1381:RSSCHI>2.0.CO;2

Liston, G. E., & Elder, K. (2006). A distributed snow-evolution modeling system (SnowModel). *Journal of Hydrometeorology*, *7*(6), 1259–1276. https://doi.org/10.1175/JHM548.1

Liston, G. E., & Hiemstra, C. A. (2011). The changing cryosphere: Pan-Arctic snow trends (1979–2009). *Journal of Climate*, *24*(21), 5691–5712. https://doi.org/10.1175/JCLI-D-11-00081.1

Luce, C. H., & Tarboton, D. G. (2004). The application of depletion curves for parameterization of subgrid variability of snow. *Hydrological Processes*, *18*(8), 1409–1422. https://doi.org/10.1002/hyp.1420

Luce, C. H., Tarboton, D. G., & Cooley, K. R. (1999). Sub-grid parameterization of snow distribution for an energy and mass balance snow cover model. *Hydrological Processes*, *13*(12-13), 1921–1933. https://doi.org/10.1002/(SICI)1099-1085(199909)13:12/13<1921::AID-HYP867>3.0.CO;2-S

MacFerrin, M., Machguth, H., van As, D., Charalampidis, C., Stevens, C. M., Heilig, A., et al. (2019). Rapid expansion of Greenland's low-permeability ice slabs. *Nature*, *573*(7774), 403–407. https://doi.org/10.1038/s41586-019-1550-3

Marcianesi, G., Aulicino, P., & Wadhams, P. (2021). Arctic sea ice and snow cover albedo variability and trends during the last three decades. *Polar Science*, *28*, 100617. https://doi.org/10.1016/j.polar.2020.100617

Marsh, P., & Woo, M.-K. (1984a). Wetting front advance and freezing of meltwater within a snow cover: 1. Observations in the Canadian Arctic. *Water Resources Research*, *20*(12), 1853–1864. https://doi.org/10.1029/WR020i012p01853

Marsh, P., & Woo, M.-K. (1984b). Wetting front advance and freezing of meltwater within a snow cover: 2. A simulation model. *Water Resources Research*, *20*(12), 1865–1874. https://doi.org/10.1029/WR020i012p01865

McDonnell, J. J., Spence, C., Karran, D. J., Van Meerveld, H. J., & Harman, C. J. (2021). Fill-and-spill: A process description of runoff generation at the scale of the beholder. *Water Resources Research*, *57*(5), e2020WR027514. https://doi.org/10.1029/2020WR027514

Mellor, M. (1965). *Optical measurements on snow* (Vol. 169). U.S. Army Materiel Command, Cold Regions Research & Engineering Laboratory.

Nolan, M., Larsen, C., & Sturm, M. (2015). Mapping snow depth from manned aircraft on landscape scales at centimeter resolution using structure-from-motion photogrammetry. *The Cryosphere*, *9*(4), 1445–1463. https://doi.org/10.5194/tc-9-1445-2015

Parajuli, A., Nadeau, D. F., Anctil, F., & Alves, M. (2021). Multilayer observation and estimation of the snowpack cold content in a humid boreal coniferous forest of eastern Canada. *The Cryosphere*, *15*(12), 5371–5386. https://doi.org/10.5194/tc-15-5371-2021

Park, H., Launiainen, S., Konstantinov, P. Y., Iijima, Y., & Fedorov, A. N. (2018). Modeling the effect of moss cover on soil temperature and carbon fluxes at a tundra site in northeastern Siberia. *Journal of Geophysical Research: Biogeosciences*, *123*(9), 3028–3044. https://doi.org/10.1029/2018JG004491

Parr, C., Sturm, M., & Larsen, C. (2020). Snowdrift landscape patterns: An Arctic investigation. *Water Resources Research*, *56*(12), e2020WR027823. https://doi.org/10.1029/2020WR027823

Perovich, D. K. (2007). Light reflection and transmission by a temperate snow cover. *Journal of Glaciology*, *53*(181), 201–210. https://doi.org/10.1088/1748-9326/aaefb3

Perovich, D. K., Grenfell, T. C., Light, B., & Hobbs, P. V. (2002). Seasonal evolution of the albedo of multiyear Arctic sea ice. *Journal of Geophysical Research*, *107*(C10), SHE-20-1–SHE-20-13. https://doi.org/10.1029/2000JC000438

Perovich, D. K., Meier, W., Tschudi, M., Hendricks, S., Petty, A. A., Divine, D., et al. (2020). *Sea ice*. Arctic Report Card 2020 (Vol. *10*). NOAA. https://doi.org/10.25923/n170-9h57

Petrich, C., Eicken, H., Polashenski, C., Sturm, M., Harbeck, J., Perovich, D., & Finnegan, D. (2012). Snow dunes: A controlling factor of melt pond distribution on Arctic sea ice. *Journal of Geophysical Research*, *117*(C9), C09029. https://doi.org/10.1029/2012JC008192

Pflug, J., & Lundquist, J. (2020). Inferring distributed snow depth by leveraging snow pattern repeatability: Investigation using 47 lidar observations in the Tuolumne watershed, Sierra Nevada, California. *Water Resources Research*, *56*(9), e2020WR027243. https://doi.org/10.1029/2020WR027243

Polashenski, C. M., Golden, K. M., Perovich, D. K., Skyllingstad, E., Arnsten, A., Stwertka, C., & Wright, N. (2017). Percolation blockage: A process that enables melt pond formation on first year Arctic sea ice. *Journal of Geophysical Research: Oceans*, *122*(1), 413–440. https://doi.org/10.1002/2016JC011994

Pomeroy, J. W., Hanson, S., & Faria, D. (2001). Small-scale variation in snowmelt energy in a boreal forest: An additional factor controlling depletion of snow cover. *Proceedings of the eastern snow conference* (Vol. 58, pp. 85–96).

Pomeroy, J. W., Toth, B., Granger, R. J., Hedstrom, N. R., & Essery, R. L. H. (2003). Variation in surface energetics during snowmelt in a subarctic mountain catchment. *Journal of Hydrometeorology*, *4*(4), 702–719. https://doi.org/10.1175/1525-7541(2003)004<0702:VISEDS>2.0.CO;2

QGIS 3.12.1-București. (2020). QGIS API documentation. 3.12.1-București (121cc00ff0). Retrieved from https://api.qgis.org/api/3.12/

Sánchez, J.-P., & McInnes, C. R. (2015). Optimal sunshade configurations for space-based geoengineering near the Sun-Earth L1 point. *PLoS One*, *10*(8), e0136648. https://doi.org/10.1371/journal.pone.0136648

Schlögl, S., Lehning, M., & Mott, R. (2018). How are turbulent sensible heat fluxes and snow melt rates affected by a changing snow cover fraction? *Frontiers in Earth Science*, *6*(154). https://doi.org/10.3389/feart.2018.00154

Schwerdtfecer, P. (1963). The thermal properties of sea ice. *Journal of Glaciology*, *4*(36), 789–807. https://doi.org/10.3189/S0022143000028379

Sexstone, G. A., Penn, C. A., Liston, G. E., Gleason, K. E., Moeser, C. D., & Clow, D. W. (2020). Spatial variability in seasonal snowpack trends across the Rio Grande headwaters (1984–2017). *Journal of Hydrometeorology*, *21*(11), 2713–2733. https://doi.org/10.1175/JHM-D-20-0077.1

Spence, C., & Woo, M.-K. (2003). Hydrology of subarctic Canadian shield: Soil-filled valleys. *Journal of Hydrology*, *279*(1–4), 151–166. https://doi.org/10.1016/S0022-1694(03)00175-6

Stone, R. S., Dutton, E. G., Harris, J. M., & Longenecker, D. (2002). Earlier spring snowmelt in northern Alaska as an indicator of climate change. *Journal of Geophysical Research*, *107*(D10), ACL-10. https://doi.org/10.1029/2000JD000286

Sturm, M., & Holmgren, J. (1993). Rain-induced water percolation in snow as detected using heat flux transducers. *Water Resources Research*, *29*(7), 2323–2334. https://doi.org/10.1029/93WR00609

Sturm, M., & Holmgren, J. (1998). Differences in compaction behavior of three climate classes of snow. *Annals of Glaciology*, *26*, 125–130. https://doi.org/10.3189/1998AoG26-1-125-130

Sturm, M., & Holmgren, J. (2018). An automatic snow depth probe for field validation campaigns. *Water Resources Research*, *54*(11), 9695–9701. https://doi.org/10.1029/2018WR023559

Sturm, M., & Liston, G. E. (2021). Revisiting the global seasonal snow classification: An updated dataset for Earth system applications. *Journal of Hydrometeorology*, *22*(11), 2917–2938. https://doi.org/10.1175/JHM-D-21-0070.1

Sturm, M., Schimel, J., Michaelson, G., Welker, J. M., Oberbauer, S. F., Liston, G. E., et al. (2005). Winter biological processes could help convert Arctic tundra to shrubland. *BioScience*, *55*(1), 17–26. https://doi.org/10.1641/0006-3568(2005)055[0017:WBPCHC]2.0.CO;2

Sturm, M., & Stuefer, S. (2013). Wind-blown flux rates derived from drifts at arctic snow fences. *Journal of Glaciology*, *59*(213), 21–34. https://doi.org/10.3189/2013JoG12J110

Sturm, M., & Wagner, A. (2010). Using repeated patterns in snow distribution modeling: An Arctic example. *Water Resources Research*, *46*(12), W12549. https://doi.org/10.1029/2010WR009434

Trochim, E. D., Jorgenson, M. T., Prakash, A., & Kane, D. L. (2016). Geomorphic and biophysical factors affecting water tracks in northern Alaska. *Earth and Space Science*, *3*(3), 123–141. https://doi.org/10.1002/2015EA000111

van der Valk, L. D., Teuling, A. J., Girod, L., Pirk, N., Stoffer, R., & van Heerwaarden, C. C. (2022). Understanding wind-driven melt of patchy snow cover. *The Cryosphere*, *16*(10), 4319–4341. https://doi.org/10.5194/tc-16-4319-2022

Van Mullem, A., & Garen, D. (2004). Chapter 11 snowmelt. In *USDA NRCS Part 630 hydrology national engineering handbook* (p. 210). VI-NEH.

Vérin, G., Domine, F., Babin, M., Picard, G., & Arnaud, L. (2022). Metamorphism of snow on Arctic sea ice during the melt season: Impact on spectral albedo and radiative fluxes through snow. *The Cryosphere*, *16*(9), 3431–3449. https://doi.org/10.5194/tc-16-3431-2022

Visser, F., Woodget, A., Skellern, A., Forsey, J., Warburton, J., & Johnson, R. (2019). An evaluation of a low-cost pole aerial photography (PAP) and structure from motion (SfM) approach for topographic surveying of small rivers. *International Journal of Remote Sensing*, *40*(24), 9321–9351. https://doi.org/10.1080/01431161.2019.1630782

Walker, D. A., Everett, K. R., Webber, P. J., & Brown, J. (1980). *Geobotanical Atlas of the Prudhoe Bay region*. CRREL Report 80-14. US Army Corps of Engineers.

Warren, S. (1982). Optical properties of snow. *Reviews of Geophysics*, *20*(1), 67–89. https://doi.org/10.1029/RG020i001p00067

Washburn, A. L. (1956). Classification of patterned ground and review of suggested origins. *Geological Society of America Bulletin*, *67*(7), 823–866. https://doi.org/10.1130/0016-7606(1956)67[823:COPGAR]2.0.CO;2

Webb, R. W., Wigmore, O., Jennings, K., Fend, M., & Molotch, N. P. (2020). Hydrologic connectivity at the hillslope scale through intra-snowpack flow paths during snowmelt. *Hydrological Processes*, *34*(7), 1616–1629. https://doi.org/10.1002/hyp.13686

Webster, M., Holland, M., Wright, N., Hendricks, S., Hutter, N., Itkin, P., et al. (2022). Spatiotemporal evolution of melt ponds on Arctic sea ice: MOSAiC observations and model results. *Elementa: Science of the Anthropocene*, *10*(1), 000072. https://doi.org/10.1525/elementa.2021.000072

Weller, G., & Holmgren, B. (1974). The microclimates of the Arctic tundra. *Journal of Applied Meteorology and Climatology*, *13*(8), 854–862. https://doi.org/10.1175/1520-0450(1974)013<0854:TMOTAT>2.0.CO;2

Woo, M.-K., Heron, R., & Marsh, P. (1982). Basal ice in high Arctic snowpacks. *Arctic and Alpine Research*, *14*(3), 251–260. https://doi.org/10.2307/1551157